Article

Study of Panel Zone Behavior in Interior Beam–Column Joints with Reduced Beam Section (RBS)

Ke-Jia Yang [1], Yang Yang [2,3], Heng Ye [2,4], Wei Li [2,4,*] and Zhao-Yu Yang [2,5,*]

1 College of Civil Engineering and Architecture, Taizhou University, Taizhou 318000, China; yangkejia99@163.com
2 College of Civil Engineering and Architecture, Wenzhou University, Wenzhou 325035, China; yang2452743748@163.com (Y.Y.); 17557296753@163.com (H.Y.)
3 Wenzhou Chengjian Grput Co., Ltd., Wenzhou 325000, China
4 Key Laboratory of Engineering and Technology for Soft Soil Foundation and Tideland Reclamation of Zhejiang Province, Wenzhou 325035, China
5 Wenzhou Engineering Technical Research Center on Building Energy Conservation and Emission Reduction & Disaster Prevention and Mitigation, Wenzhou 325035, China
* Correspondence: weili@wzu.edu.cn (W.L.); yangzhaoyu20232023@163.com (Z.-Y.Y.)

Abstract: Based on the post-earthquake investigation of the Beiling and Hanshen earthquakes, many welded rigid beam–column joints were found to exhibit brittle failure. The failure modes of the joint region and the overall steel frame structure under the action of the earthquake need to be studied. The seismic performance of different types of weakened beam-end interior joints was investigated. The finite element method was verified by high-strength steel beam–column joint tests conducted by our research team. Finite element modeling of weakened steel beam flanges and weakened steel beam web joints was carried out based on the validated finite element modeling method. The joints were studied and analyzed using seismic parameters such as joint stress clouds, equivalent story shear–inter-story displacement ratio curves, panel zone bending moment–shear ratio curves, ductility, stiffness, and energy dissipation. The results of this study showed that honeycomb open hole-type joints exhibit a better deformation and energy dissipation capacity compared to open circular web hole-type joints. However, their load carrying capacity is reduced, which is mainly due to the larger area of the web openings. Additionally, double reduced beam section (DRBS) joints exhibit superior seismic performance and plastic hinge outward movement characteristics compared to single reduced beam section (RBS) joints. It was also found that the deformation and energy dissipation of DRBS joints and steel beam honeycomb hole-type joints are mainly borne by the beams, with the panel zone's participation in energy dissipation accounting for a smaller proportion of the energy.

Keywords: beam–column joints; reduced beam section; panel zone; seismic performance; moment connections

1. Introduction

Compared with traditional reinforced concrete beam–column joints, steel structure beam–column joints have the advantages of light self-weight, high strength, and strong forming ability [1–8]. Nowadays, steel structure joints are also widely used globally, especially in large-scale factories and high-rise buildings. The seismic performance of steel beam–column joints has been extensively studied worldwide at home and abroad, mainly including experimental, theoretical, and finite element aspects.

For the experimental studies, Tsai et al. [9] conducted cyclic load tests on 10 joints with bolted web welded wing flanges (BWWFs), mainly to investigate the effects of the plastic modulus ratio of the beam flange to the full cross-section of the beam, the additional bolts in the web, the web filler welds, and the strength of the panel zone on the joint performance. The authors suggest that the panel zone yield capacity is 0.8 times the beam yield capacity

when the panel zone and beam inelastic deformation develop synchronously, and the two exhibit a better co-deformation ability. Zhou et al. [10], who studied the effect of different types of steel joints (common joints (CJs), steel beam weakening joints (RJs), and cover joints (CPJs)) on the seismic performance of frames. The study was analyzed in terms of the failure mode, load–displacement, and strain development. The experimental results show that the damage to the steel frame specimens is mainly concentrated in the first level of the beam–column joints. Plastic hinges can be used to achieve outward movement by strengthening and reducing the steel beam flanges, which significantly improves the seismic capacity of the structure. In addition, to investigate the effect of out-of-plane loading on the seismic performance of steel joints, Pan et al. [11] designed four spatial H-section steel beam–column joint specimens with different configurations, applying a constant anti-symmetrical load at the weak axis beam end and an anti-symmetrical cyclic load at the strong axis beam end. The effects of the out-of-face loading of steel frames on the damage modes, deformation capacity, load carrying capacity, and energy dissipation properties of the panel zones were investigated. Thereafter, Pan et al. [12] proposed a modified calculation equation of elastic stiffness considering the influence of the two-way bending of the joint domain. In this paper, it was verified by experiments and a finite element analysis that the modified equation considering the influence of bidirectional bending can more accurately calculate the elastic stiffness value of the joint domain, to obtain a more accurate equivalent shear deformation value of the joint domain in the elastic stage, and then to obtain more accurate calculation results in the overall structural analysis considering the deformation of the joint domain.

In the study of joint tests, scholars from various countries have also studied the stress mechanism and bearing capacity prediction equation of joints. Brandonisio et al. [13] introduced the mechanical mechanism of nodal domains and discussed the design methods of nodal domains in American and European codes. The test results show that the American specification is more in line with the theoretical standards. Thereafter, Reza Amani et al. [14] proposed analytical and numerical models of double-web columns to predict the local bending of beam flanges. The local flange bending is directly related to the type of column section. Aiming at this problem, Reza et al. proposed the relationship between H-shaped columns by using the yield linear theory, analysis, and experimental observation. The comparison of the experimental and numerical results with the AISC specification shows that the established equations exhibit good accuracy and reliability. Two different equations for calculating the local bending of the column flange are proposed because the reliable and economical calculation equation for the seismic requirements of the column flange with double webs is not considered. Compared with the finite element results, one is conservative and the other is accurate. Finally, based on the local flange bending relationship considering the seismic requirements, the minimum thickness requirement equation of the double-web column is proposed. Moreover, Wang et al. [15] studied the yield process and failure mechanism of the joint region of the steel frame, analyzed the influence of the shear yield of the joint region on the lateral displacement of the frame, and deduced the equation for calculating the thickness of the joint region of the steel frame based on the finite element model. Ren et al. [16] investigated the influence of the flange plate length, thickness, and other parameters on the mechanical properties of joints and joint domain, and carried out a numerical simulation. The results show that the longer the length of the flange plate, the greater the influence on the shear force of the joint domain, and the thickness of the web of the joint domain also needs to be increased.

It may be easier to analyze the seismic performance of steel beam–column joints directly in the laboratory, but the preliminary preparation of steel beam–column joint specimens is time-consuming, including the design of components such as steel beams, columns, bolts, and reinforcing ribs, as well as the production and assembly of these components, and the cost is high. On the other hand, the loading process cannot clearly reflect the stress changes in each component. Therefore, finite elements have been widely used in seismic studies of steel joints. For example, to study the inelastic behavior of the

panel zone and the influence of the panel zone yield on the fracture possibility of welded–bolted joints, El-Tawil et al. [17] used finite element analysis to explore the influence of the panel zone yield on bolted–welded steel joint fractures, and the main parameters were panel zone thickness, beam cross-section height, and beam flange thickness. The results show that the plastic rotation angle of the beam is less demanding in the connection of the weak joint region, but the stress condition is more serious under the higher plastic rotation angle of the connection. Therefore, although the panel zone can effectively improve the ductility of the overall connection, a weak panel zone may also lead to a greater possibility of brittleness or ductile fracture at the higher plastic corners of the connection. Therefore, the AICS specification is not applicable to the calculation method of the yield bearing capacity of the panel zone.

Yang et al. [18] used ANSYS 2021 finite element software to carry out refined finite element modeling of axil plate reinforced joints, rib plate reinforced joints, and cover plate reinforced joints, and investigated the mechanical properties of the panel zone under the action of low circumferential repetitive loading. The results show that the length of the reinforcing plate has a great influence on the mechanical properties of the panel zone of steel frames, and the plastic hinges essentially appeared far away from the weld position of the beam end when the length of the axillary plate was 0.6–0.7 times the height of the beam, the length of the rib plate was 0.6–0.8 times the height of the beam, and the length of the cover plate was 0.5–0.9 times the height of the beam. In the study of steel beam weakened joints, Chen et al. [19] conducted a finite element seismic performance analysis for weakened flange joints with different thicknesses of the panel zone. Subsequently, a comparative study was carried out with a normal joint, and the test results showed that for the normal joint (NBJ), the thicker the panel zone is, the less likely the joint stress concentration phenomenon is to be formed in the panel zone, and the flange at the beam end connected with the column is more likely to be the first part of the stress concentration to occur; for the weakened flange joint (RNJ), the thicker the panel zone is, the more likely it is that the stress concentration will form in the weakened flange, which protects the panel zone and beam–column connection parts. In addition, Deylami et al. [20] investigated the seismic performance of six beam weakened flange joints using ANSYS finite element software.

At present, multi- and high-level steel frame beam–column connections are mainly used for rigid connections; traditional beam–column rigid connections have all-welded joints, bolted–welded hybrid joints, and all-bolted joints and another three forms of connections. In seismic structural design, including a strengthened panel zone and weakened steel beam are two key issues. In recent years, scholars at home and abroad, for these three types of connection joints and these two types of structural measures, have carried out a large amount of experimental research and numerical simulations, and have obtained fruitful research results, but for the panel zone's weakened welded steel joint force performance, there is still insufficient research. In this paper, the numerical model is verified in terms of the accuracy and effectiveness of the finite element model. Then, the low-cycle reciprocating loading numerical analysis of ordinary joints and steel beam weakened joints is carried out to study the influence of different connection methods on the mechanical properties of the panel zone.

2. Validation of Finite Element Model

2.1. The Design of the Joint

Our research team carried out cyclic loading tests to investigate their seismic behavior [21]. The specimen is installed on the loading frame as a whole. The bottom of the square steel tube column is connected to the ground beam with hinged support, and the top is also connected to the extended transfer head of the loading frame through the hinged support to ensure that the beam end can rotate during the loading process of the specimen. There is an out-of-plane constraint folding plate on the lower side of the beam-end of the specimen far away from the column. A 60-ton jack is installed at the upper part of the beam end, and a vertical load is applied to the specimen. The steel used for the beams and

columns was Q235 steel and Q690 steel plate, respectively. The weld used in the specimen model is shown in Figure 1. The strength of the bolt for the connections is grade 10.9.
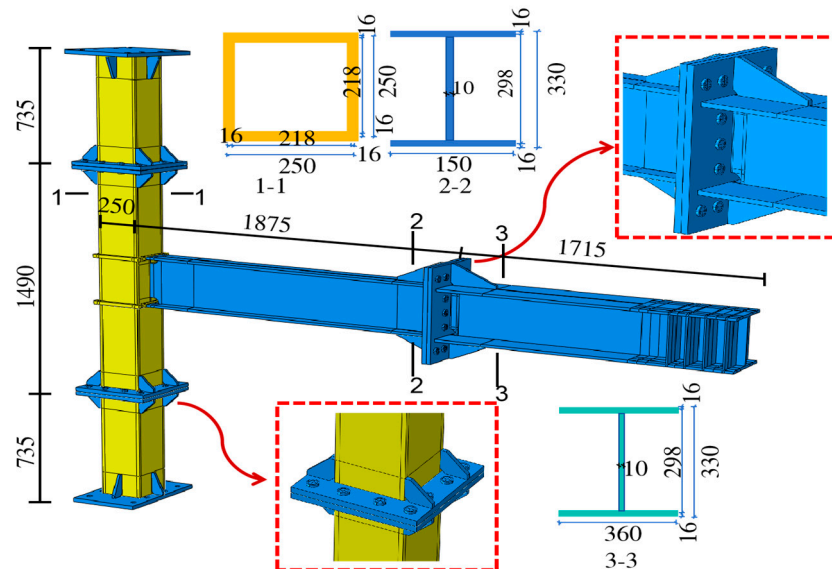

Figure 1. Detailed drawing of specimen dimensions (mm).

2.2. Loading System

In this study, beam-end displacement control loading was used, and the inter-story displacement angle was used as the control parameter. The inter-story displacement angle was 0.5%, 1.0%, 1.5%, 2.0%, 3.0%, 4.0%, 5.0%, and 6.0%. Each stage was loaded twice. When the bearing capacity was reduced to less than 85% of the peak bearing capacity or the specimen was damaged, the loading was stopped. The loading system used in the test is shown in Figure 2.
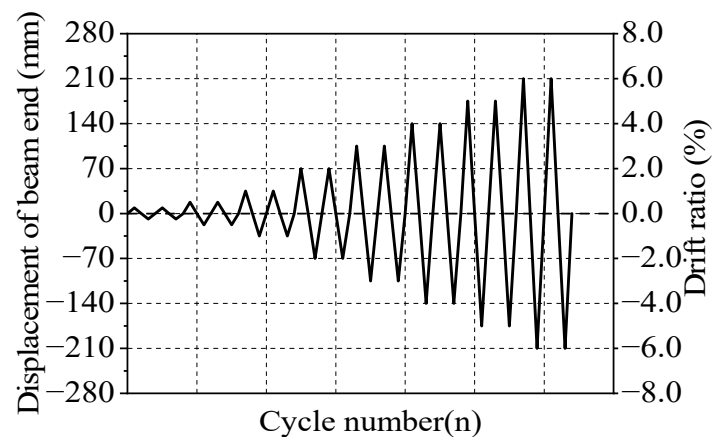

Figure 2. Specimen OJ and HJ-1 test loading system.

2.3. Constitutive Performance Parameters of Steel

In this study, the finite element software ABAQUS 2021 is used for simulation and verification. Specimen OJ consisted of a traditionally welded ordinary steel joint with steel type Q235 and joint HJ-1 was a traditionally welded high-strength steel joint with steel type Q690.

The universal testing machine was used with the Q235 and Q690 specimens for the tensile test, and the performance of each specimen's material, including the Q235 model with a thickness of 10 mm and 16 mm and the Q690 model with a thickness of 10 mm, 16 mm, and 22 mm, is listed in Table 1. According to Equations (1)–(3), the converted real relationship of the stress–strain as well as the constitutive relationship of each thickness of steel is input into the finite element model. Therefore, it is necessary to convert the test data into the form required by ABAQUS before using it. The conversion results are shown in Table 2.

Table 1. Table of mechanical properties of steel for testing.

Steel Type	Plate Thickness t (mm)	Yield Strength f_y (MPa)	Yield Strain ε_y	Tensile Strength f_u (MPa)	Ultimate Strain ε_u	Rupture Strength f_{st} (MPa)	Rupture Strain ε_{st}	Flexure Ratio
Q235	10	397.7	0.002	533.9	0.193	385.3	0.503	0.74
	16	289.2	0.002	469.1	0.073	328.7	0.420	0.62
Q690	10	326.7	0.002	516.0	0.223	360.8	0.412	0.69
	16	705.7	0.004	758.8	0.079	422.9	0.284	0.93
	22	938.0	0.005	1006.7	0.054	657.4	0.307	0.93

Table 2. Steel intrinsic structure data for numerical model.

Steel Type	Plate Thickness t (mm)	Elasticity Modulus E (MPa)	Yield Strength f_y (MPa)	Yield Strain ε_y	Tensile Strength f_u (MPa)	Ultimate Strain ε_u	Rupture Strength f_{st} (MPa)	Rupture Strain ε_{st}
Q235	10	207,000	398.60	0.00233	639.35	0.17350	578.89	0.40712
	16	204,330	289.70	0.00184	503.47	0.7013	466.69	0.35064
Q690	10	186,270	327.43	0.00234	630.65	0.20071	510.72	0.34464
	16	204,030	708.33	0.00376	818.55	0.07545	536.43	0.24908
	22	204,400	942.57	0.00485	1060.77	0.05245	859.24	0.26740

Conversion equation between real and nominal stresses:

$$\sigma_t = \sigma_{nom}(1 + \varepsilon_{nom})\sigma_t \tag{1}$$

Conversion equation between real and nominal strains:

$$\varepsilon_t = \ln(1 + \varepsilon_{nom}) \tag{2}$$

The deformation of a material consists of elastic and plastic deformation, so the plastic strain of the material is as follows:

$$\varepsilon_p = |\varepsilon_t| - |\sigma_t|/E \tag{3}$$

Note: E is the elastic modulus; σ_t is the real stress; σ_{nom} is the nominal stress; ε_t is the real strain; ε_{nom} is the nominal strain; ε_p is the plastic strain.

The numerical simulation of the principal structure uses a triple-fold model considering the strengthening phase and the falling section, and the principal relationship for the numerical simulation inputs for the Q235 and Q690 steels are shown in the stress–strain relationship in Figure 3.
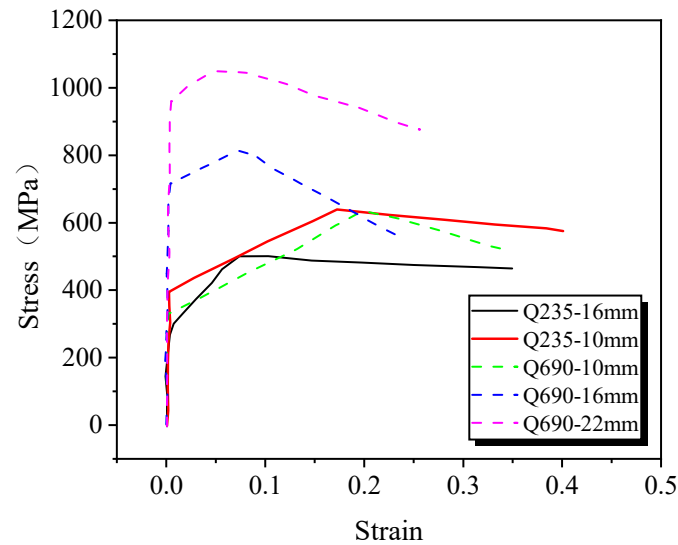
Figure 3. Numerical model steel stress—strain relationship.

2.4. Establishment of Model Boundary Conditions and Division of the Grid

The boundary conditions and applied loads of the finite element model are shown in Figures 4 and 5. The loads applied in the model include the bolt pre-tension and the beam-end displacement load. The replaceable specimen is connected to a grade-10.9 M27 high-strength friction bolt with a preload of 290 kN. The boundary conditions are set to $U1 = U2 = U3 = 0$, $UR2 = UR3 = 0$. The lower part of the beam loading end needs out-of-plane constraints. In the test, the loading problem caused by the external deformation of the loading-end face is prevented. The boundary condition is set to $U1 = 0$, and only the X-axis displacement of the loading end is limited.
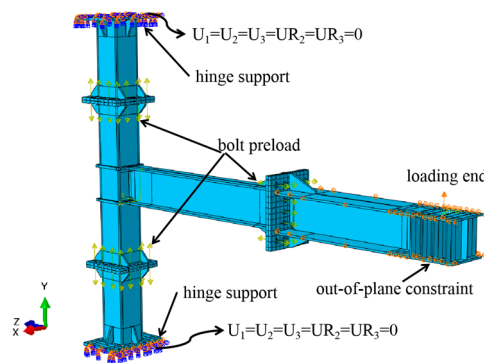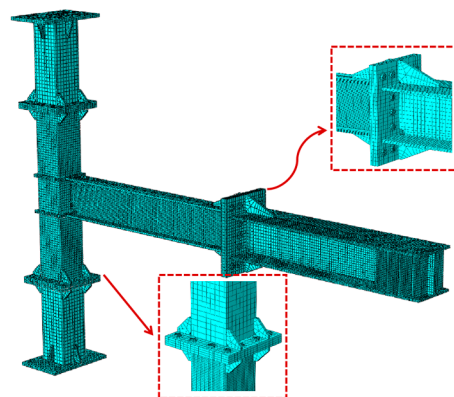

Figure 4. Boundary conditions of joint.

Figure 5. Meshing of joint.

2.5. Validation of Numerical Simulation

Figure 6 shows the comparison between the finite element failure and the experimental failure mode of the OJ specimen. When the steel girder shows slight out-of-plane deformation, and when the drift ratio is 6%, the lower flange of the steel beam near the core area cracks, the lower flange of the steel beam in Figure 6 shows a stress concentration phenomenon, and both the upper and lower flanges undergo local buckling.
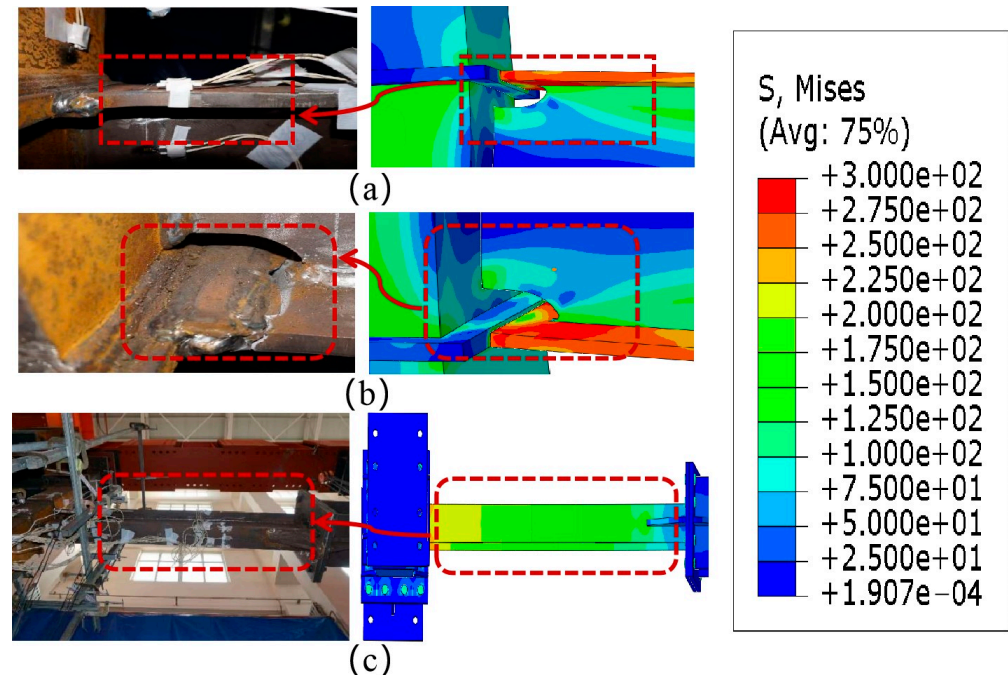

Figure 6. Comparison of the failure modes obtained by the tests and the FEM simulations. (**a**) Upper flange bulge; (**b**) lower flange; (**c**) steel beam deformation.

2.6. Comparison of Skeleton and Hysteresis Curves

It is depicted in Figure 7 that specimen OJ's test and finite element results are basically the same during the beginning stage of loading, when the story displacement ratio reaches 3%, taking into account that the steel in the strength and stiffness test process degrades faster. The positive-loading-direction finite element analysis obtained a load bearing capacity higher than the test value, and this is also the case with the negative loading direction; the overall results of the finite element analysis to obtain the hysteresis loop are more extensive. The overall results of the finite element analysis show that the hysteresis loop is fuller. For specimen HJ-1 in the initial period of loading, the finite element simulation results and the test results match well; with increasing beam-end displacement, the finite element model stiffness decrease becomes smaller than the test value. In general, the development trend of the load–slip curve of the finite element simulation is similar to the development trend of the test result curve.
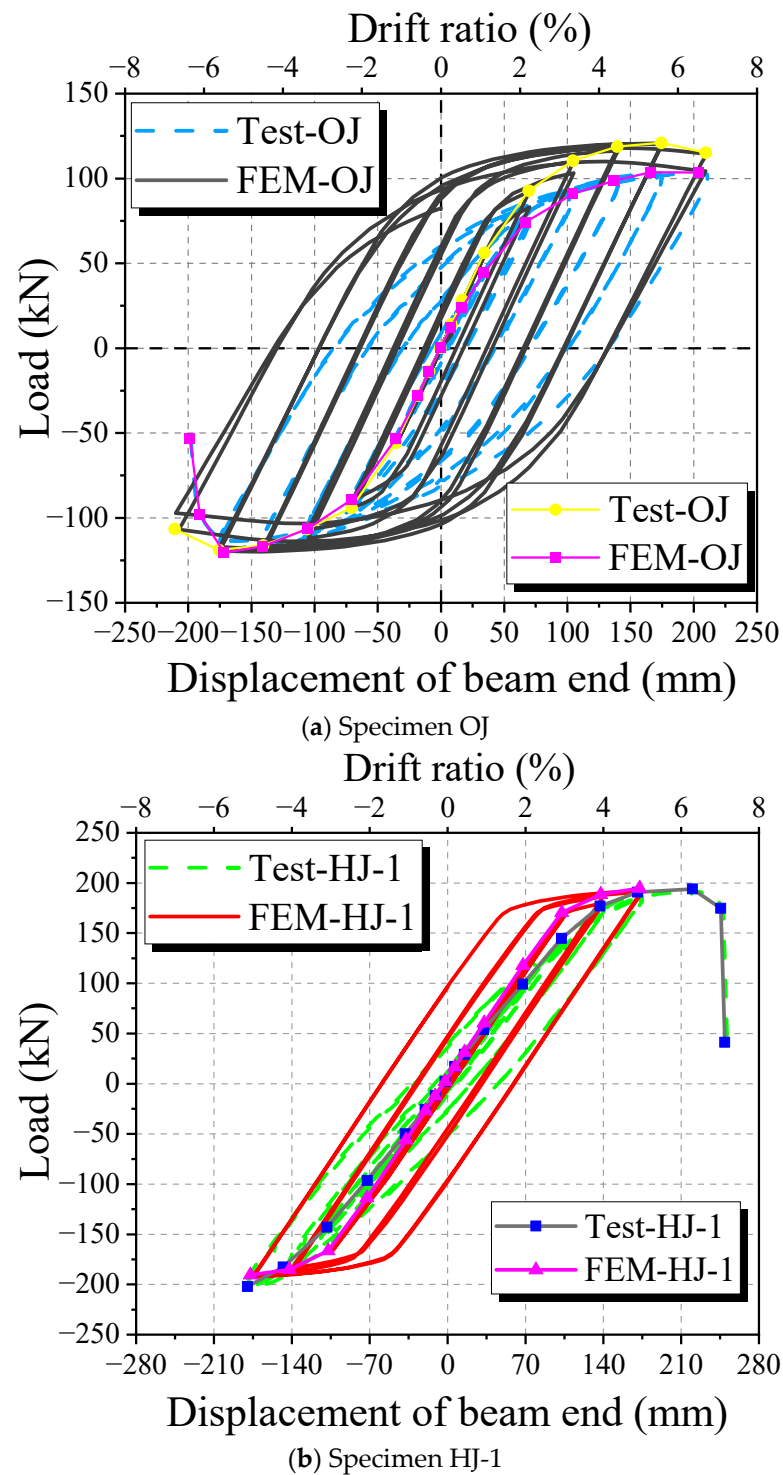
(**a**) Specimen OJ

(**b**) Specimen HJ-1

Figure 7. Contrast of skeleton and hysteresis curve.

3. Steel Beam with Weakened Beam–Column Joint

3.1. Specimen Design

The joint specimens in the beams and columns have a column height H = 3.3 m, beam span L = 7.2 m, column section: 400 × 200 × 16 × 16, beam section: 330 × 150 × 10 × 14. Five finite element models are established based on the abovementioned nodal connections; the details are given in Figures 8 and 9 and show the steel beam weakened flange joints and weakened web joints, respectively. In Table 3, T16 shows that the thickness of the panel

zone is 16 mm, BFW means beam flange weakening-type joint, and BWW is beam web opening weakening-type joint.
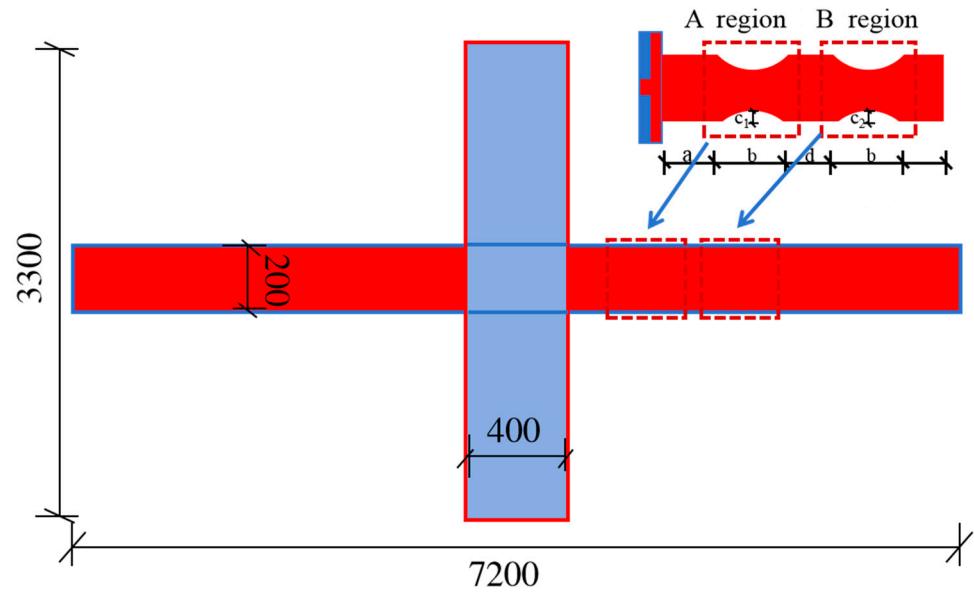

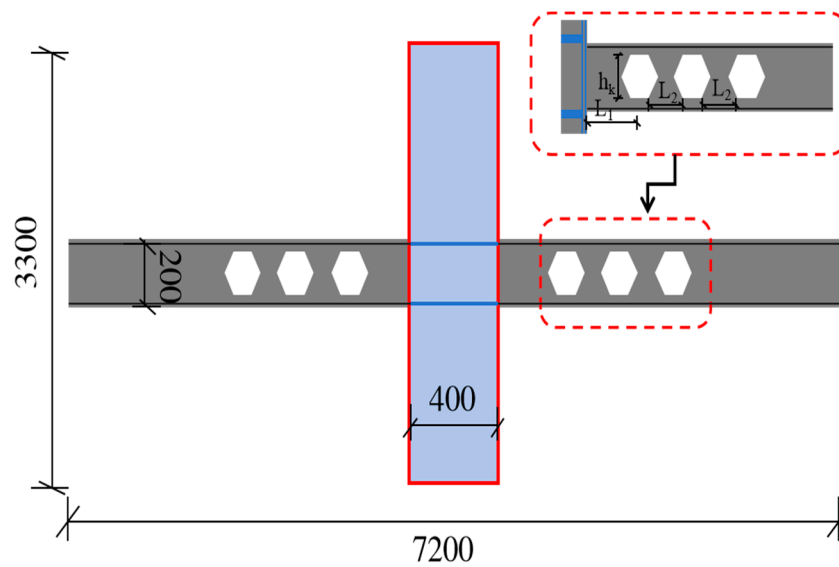**Figure 8.** Weakened DRBS steel flange joints.

Figure 9. Open cellular hole section steel web joints.

Table 3. Steel beam weakened joint specifications.

Serial Number	Specimen Number	Flange Weakening Parameters (mm)					Weakening Parameters of Web Opening (mm)			
		a	b	c_1	c_2	d	L_1	L_2	h	Opening Type
1	B345-T16									
2	B345-T16-BFW-1	75	214.5	37.5						
3	B345-T16-BFW-2	75	214.5	15	37.5	0				
4	B345-T16-BWW-1						400	150	198	Round hole
5	B345-T16-BWW-2						400	150	198	Honeycomb hole

3.2. Finite Element Modeling

3.2.1. Establishment of Finite Element Model

Figures 10 and 11 show the FEMs created using ABAQUS 2021 based on the specimen dimensions in Table 3; the beams and columns were created using C3D8R. A cell size of 50 for the columns and steel beams is sufficient to meet the accuracy requirements and computational efficiency, and this was used in this study. For the butt weld flanges of the steel beams and the lateral sides of the flanges of the steel columns, the butt welds between the transverse stiffening ribs of the panel zone and the inner side of the flanges of the columns, the fillet weld connections between the webs of the beams and the flanges of the columns, and the fillet weld connections between the transverse stiffening ribs of the panel zone and the webs of the columns, the "tie" fixed restraint was adopted. Both ends of the steel columns were fixedly restrained and the steel beam girder ends could only move in the *z*-axis direction.
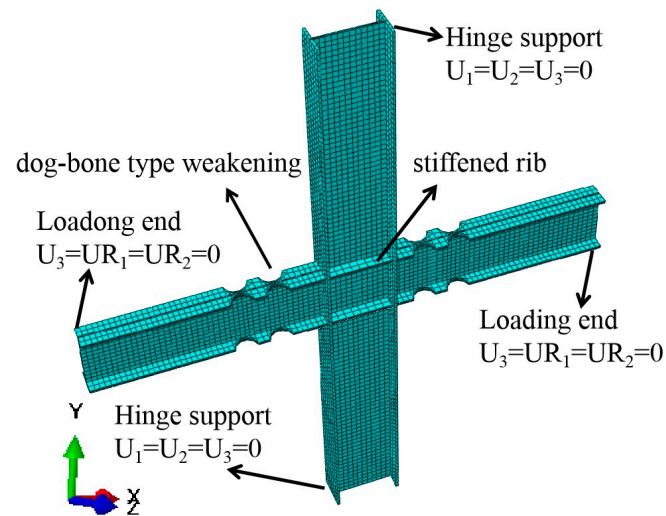

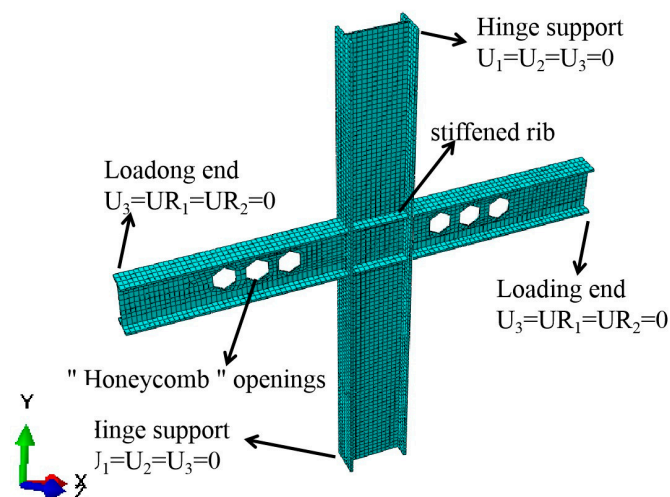**Figure 10.** Joint of weakened flange model.

Figure 11. Joint of weakened web model.

3.2.2. Introduction of Material Properties

The finite element model is a trilinear model considering the strengthening section and the descending section, as shown in Figure 12. The corresponding data obtained from the material performance test according to [22] are shown in Table 4.
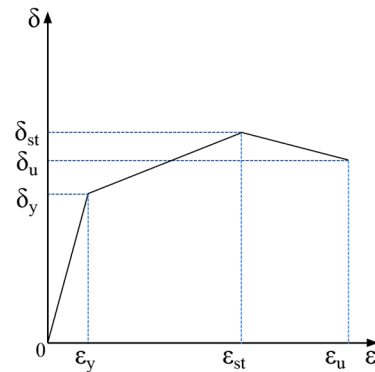

Figure 12. Stress-strain curve of steel.

Table 4. Material property parameters.

E_s	μ	σ_y	ε_y	σ_u	ε_u	σ_{st}	ε_{st}
2.05×10^5 MPa	0.3	369 N/mm^2	0.179%	514 N/mm^2	4.46%	416 N/mm^2	7.34%

Where E_s represents elastic modulus; μ represents the Poisson ratio; σ_y represents the yield strength; ε_y represents the yield strain; σ_u represents the ultimate strength; ε_u represents the ultimate strain; σ_{st} represents the ultimate strength; ε_{st} represents the ultimate strain.

3.2.3. Loading System

The finite element model adopts the full displacement control variable amplitude loading method. Referring to the American seismic code AISC341-5 [23], the loading displacement of the beam end controls the whole loading process according to the rotation angle of the beam end. The ratio of the displacement at the loading point of the beam end to the distance from the loading point of the beam end to the center line of the column is taken as nine levels. All displacement cycles are repeated two times. The specific loading system and parameter settings are shown in Table 5 and Figure 13.

Table 5. Full displacement control loading system.

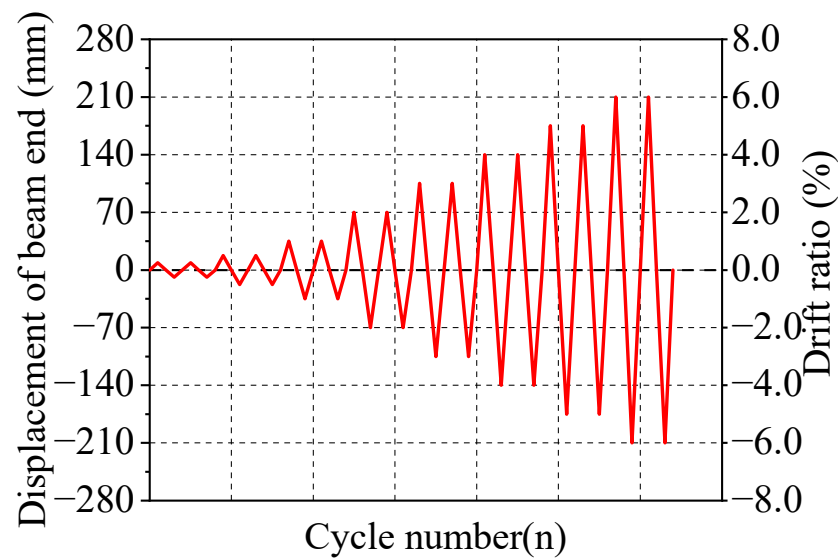| Load Level	Displacement Amplitude Δ (mm)	Cycle Index	Story Drift Ratio θ_c (rad)
1	±14.25	2	0.35%
2	±19	2	0.5%
3	±28.5	2	0.75%
4	±38	2	0.1%
5	±76	2	0.2%
6	±114	2	0.3%
7	±152	2	0.4%
8	±190	2	0.5%
9	±228	2	0.6%

Figure 13. Steel stress-strain curve.

3.3. Analysis of Finite Element Results

3.3.1. Instantaneous Stress Cloud

It can be seen from Figure 14a–d that the displacement of the beam end is in the range of 14.25–38 mm, and the B345-T16 specimen is entirely in the elastic stage. The equivalent stress of the joint domain is basically linear with the loading displacement of the beam end, and the maximum equivalent stress appears in the beam–column docking area. When the loading displacement of the beam end reaches 38 mm, due to stress concentration, plastic strain occurs at the weld toe of the reserved weld hole of the steel beam, that is, PEEQ > 0.

The displacement of the beam end gradually increases with the increase in stress. After the elastic–plastic stage, as shown in Figure 14e, slight deformation occurs in the web area of the steel beam, indicating that the specimen enters the plastic deformation stage. The displacement of the beam end continues to increase. The steel beam web in the joint domain displays obvious out-of-plane deformation, and the lower flange of the right beam and the upper flange of the left beam display local buckling. As shown in Figure 14f, when the displacement reaches 152 mm, that is, the interlayer displacement ratio reaches 4%, the steel beam produces plastic hinges and the stress in the joint domain decreases. When the specimen enters the failure stage, the bearing capacity of the joint decreases to 89.6% of the ultimate bearing capacity.

As shown in Figure 14h,i, due to the generation of plastic hinges at the beam end, the beam flange undergoes torsional deformation, the beam web undergoes out-of-plane deformation, and the joint capacity continues to decrease to 128.01 kN, and when loaded to the second turn, the capacity is 124.73 kN, which is only 77.95% of the ultimate capacity.

From Figure 15a–c, it can be seen that the earliest plastic strain occurs in the weld toe area of the weld hole of specimen B345-T16-BFW-1's steel beam, indicating that the joint enters the elastic–plastic stage. When the displacement of the beam end reaches 76 mm, the weakened region of the steel beam flange displays an obvious stress concentration which reaches the yield strength; its maximum stress value is 375.2 MPa, and the maximum stress in the center point of the panel zone is 369.67 MPa, which presents the maximum at the center point and gradually reduces the distribution law to the surroundings. At the beam-end loading of 114 mm, that is, the story displacement ratio of 4%, the specimen enters the stage of plastic deformation; the joint reaches the ultimate bearing capacity of 185 kN. As shown in Figure 15h, the steel beam flange reduction region appears to display flexural deformation, the web appears to display a bulging curvature, and the joint bearing capacity after the second turn of the loading suddenly drops to 73% of the ultimate bearing capacity, which indicates that the joint has reached the requirements of aborting

the continuation of the loading. The displacement continues to increase to 228 mm, which is 6% of the story displacement ratio, and the bearing capacity is only 111.21 kN, indicating that the joint has been damaged.
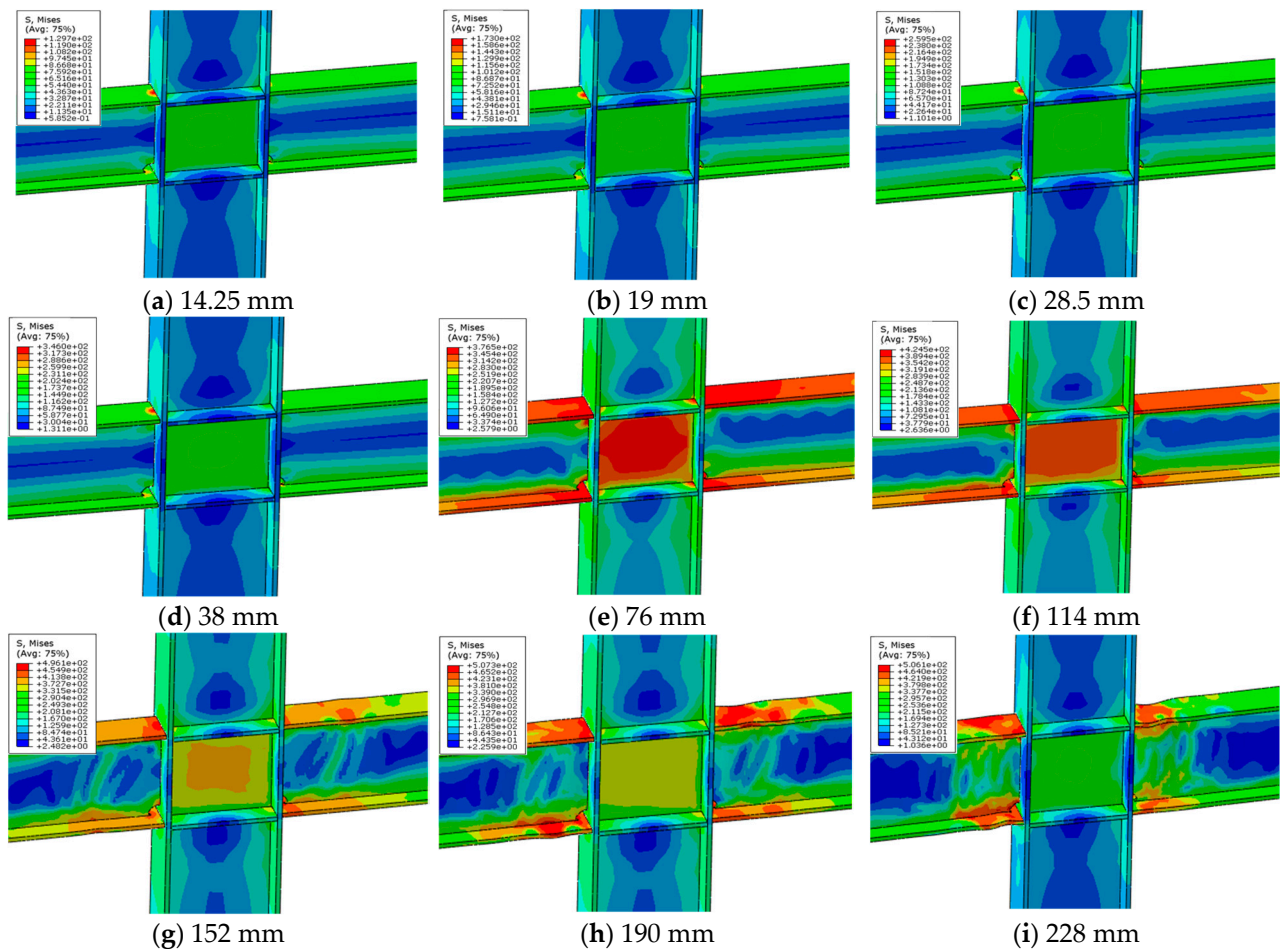

(**a**) 14.25 mm   (**b**) 19 mm   (**c**) 28.5 mm

(**d**) 38 mm   (**e**) 76 mm   (**f**) 114 mm

(**g**) 152 mm   (**h**) 190 mm   (**i**) 228 mm

Figure 14. Instantaneous stress cloud of specimen B345-T16 at each displacement loading stage.

As shown in Figure 16a–d, specimen B345-T16-BFW-2 is always in the elastic stage; when the fourth loading level is reached, i.e., at the beam-end displacement of 38 mm, the steel beam's hole weld toe part first reaches a yield strength of the maximum stress of 369.5 MPa, and at this time, the panel zone maximum stress at the center of the joint point is 308 MPa and did not display plastic deformation, indicating that the joint enters the elastic–plastic stage. As the displacement continues to increase, the panel zone exhibits plastic strain, but deformation is not observed; the steel beam flange weakening dual-region in the first part of the overall stress is less than that in the second part; the web region displays slight deformation; the story displacement ratio is 4%; and the joint reaches the ultimate load bearing capacity of 184.07 kN. With the beam-end displacement reaching 190 mm, the specimen reduction in the second region of the flange displayed obvious flexural deformation, and a large area of drumming deformation of the web plate appeared. With the girder-end displacement reaching 190 mm, the flange of the second area of the specimen reduction shows obvious buckling deformation, the web plate shows corrugated deformation with a large area of bulging deformation, the loading capacity in the second circle decreases to 85.8% of the ultimate capacity, the displacement continues to increase to 228 mm, which is 6% of the drift ratio, and the carrying capacity remains at 148.13 kN, which shows that the joint has been damaged.
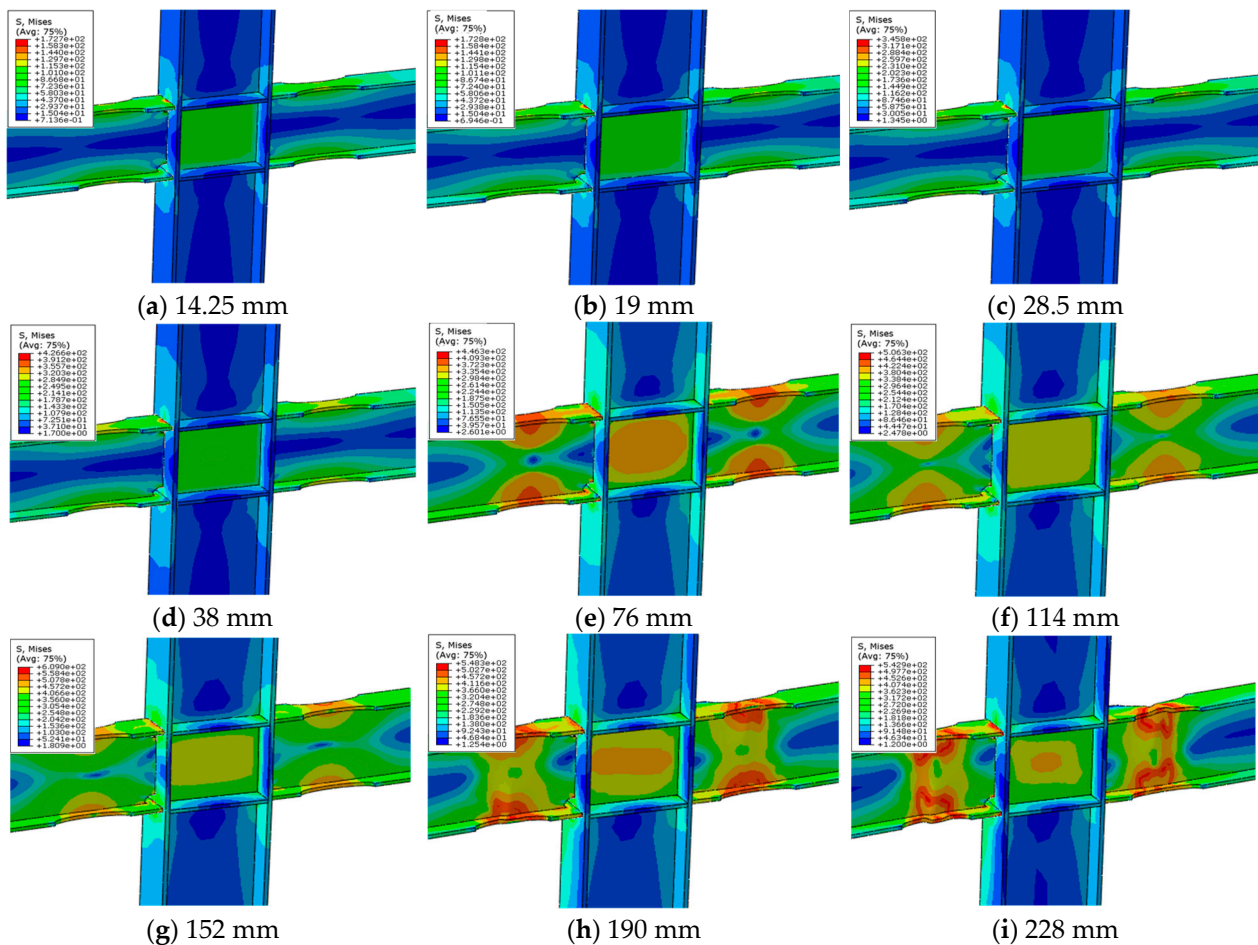
Figure 15. Instantaneous stress cloud of specimen B345-T16-BFW-1 at each displacement loading stage.

Specimens B345-T16-BWW-1 and B345-T16-BWW-2 have different forms of steel beam openings, but the damage process and the stress distribution law are the same in the loading stage, so they will not be separately elaborated. Since the beam-end displacement of the two specimens was loaded to 228 mm, the deformation was too large for convergence, so they were selected to be loaded only to 190 mm, i.e., to stop the loading after a story drift ratio of 5 percent. It can be found in Figure 17a–d that before the beam-end displacement of 38 mm, the joint is always in the elastic phase, and the panel zone and beam-end stresses essentially grow linearly as displacement increases. As the slip reaches 38 mm, i.e., the story displacement ratio is 1%, the same stress concentration occurs at the weld toe of the steel beam, and the plastic strain PEEQ > 0, indicating that the joint is in the elastic and plastic stage. With displacement loaded to 76 mm, a slight bulge occurs at the location of the web opening, and the stress at the upper flange of the first opening region of the steel beam rises sharply due to the deformation of the web, which indicates that the joint begins to display plastic deformation. The ultimate load bearing capacity of 185.20 kN is reached when the displacement ratio between the layers is 3%, and as the displacement continues to increase, the web between the honeycomb holes deforms drastically, thus causing a sudden decrease in the load capacity to 130 kN, which is 70.19% of the ultimate load capacity, and the steel beam buckles and the entire surface deforms, which indicates that the joint has been damaged.
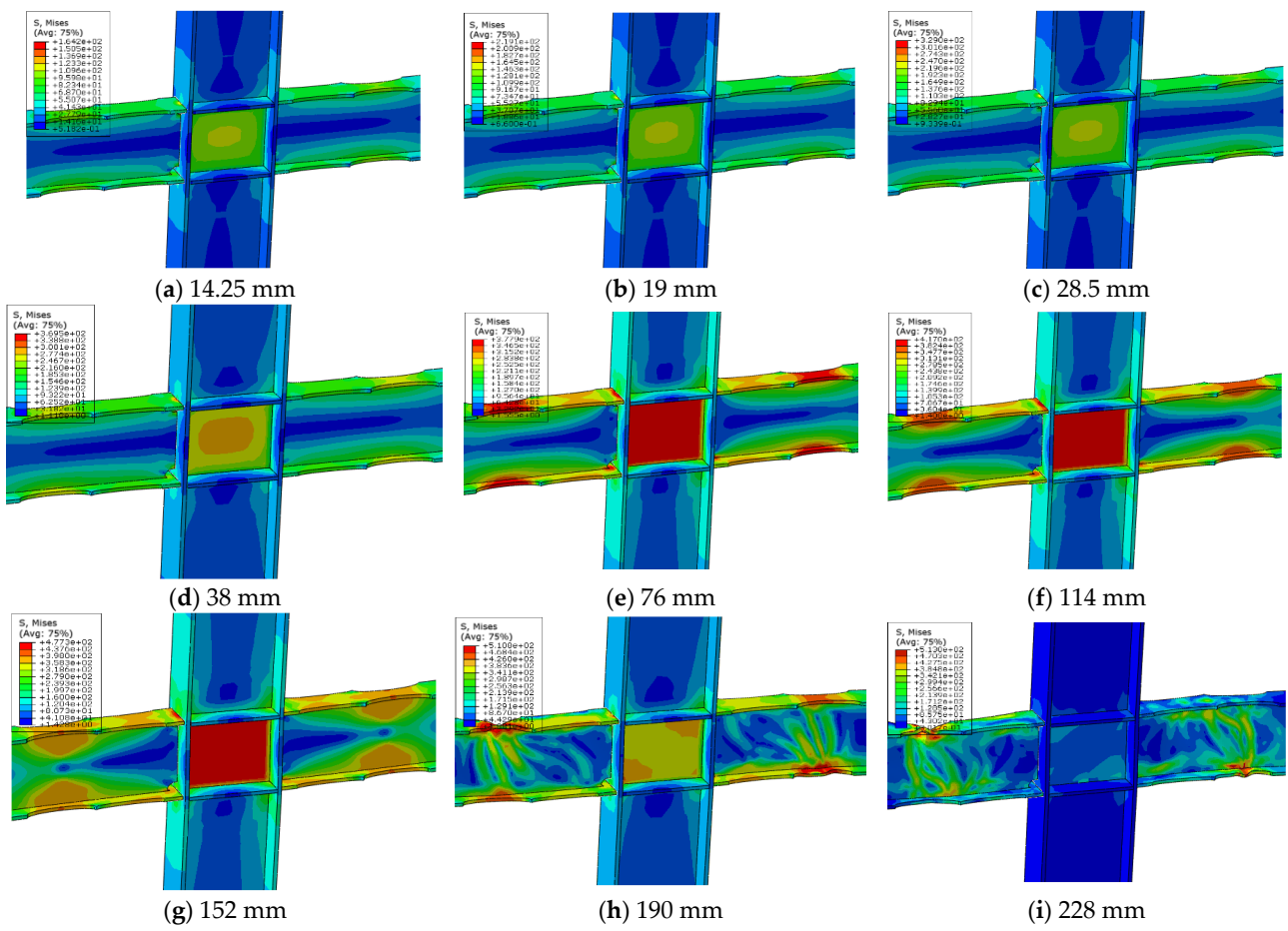
Figure 16. Stress cloud of specimen B345-T16-BFW-2 during every loading period.
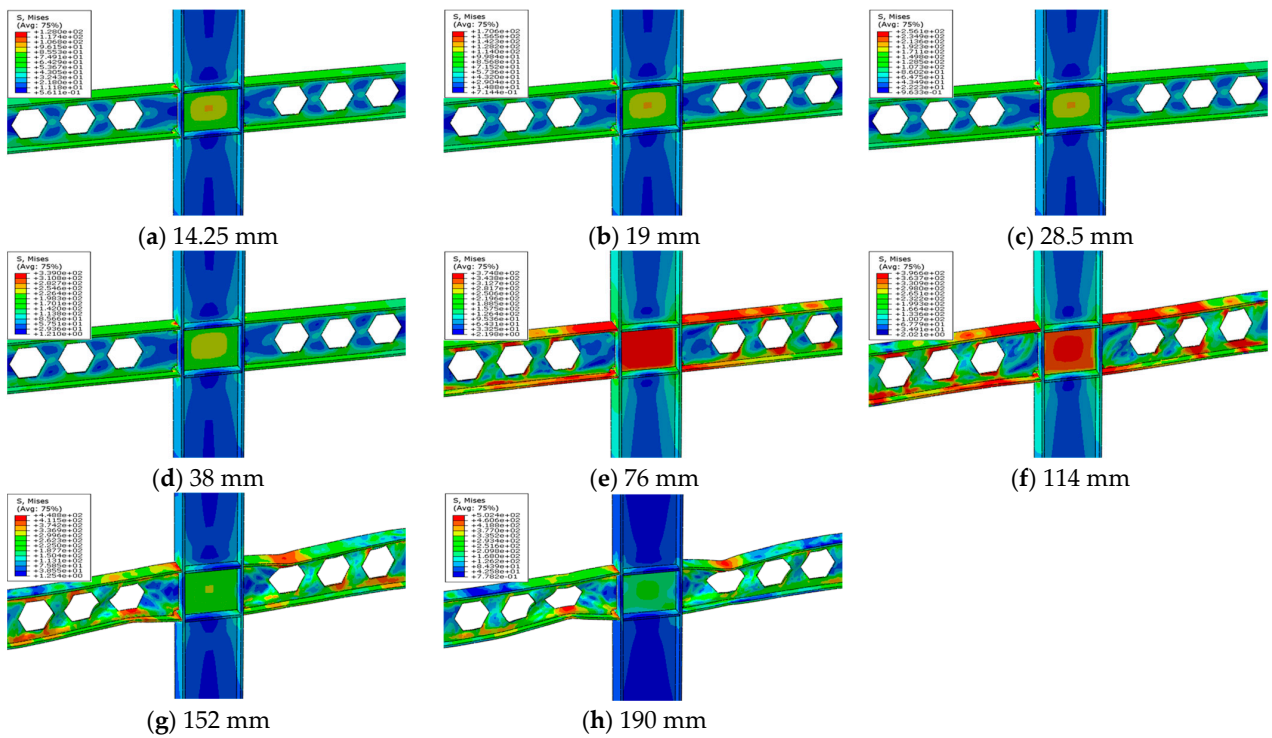

Figure 17. Stress cloud of specimen B345-T16-BWW-2 during each loading period.

3.3.2. Skeleton Curve and Shear Force–Drift Ratio Hysteresis Curve

The loading methods of the nodal specimens all display beam-end displacement-controlled loading, and the outputs in the model post-processing module are used to calculate each component of the joint story drift ratio and the panel zone shear ratio. As depicted in Figure 18, the displacement of one side beam, the other beam, and both the top and bottom of the column are output, and the story displacement ratio of the nodal model in the loading process can be calculated from these four outputs, which can be calculated using Equation (4). As shown in Figure 19, the panel zone deformation of two diagonal directions is output in the finite element post-processing module, and the panel zone shear ratio can be calculated using Equation (5). Since the finite element nodal model is loaded by displacement control at the end of the beam, the equivalent story shear at the top of the column can be calculated by the beam-end support reaction forces F_S and F_N, as detailed in Figures 18 and 20. And, in combination with the story drift ratio θ_d obtained from Equation (5), the shear–story drift ratio (Q-θ_d) curves can be obtained.

$$\theta_d = \frac{\delta_1 - \delta_2}{L} - \frac{\delta_3 - \delta_4}{H} \tag{4}$$

$$\theta_{PZ} = \frac{\delta_5 - \delta_6}{2} \frac{\sqrt{h_{pz.0}^2 + b_{pz.0}^2}}{h_{pz.0} b_{pz.0}} \tag{5}$$
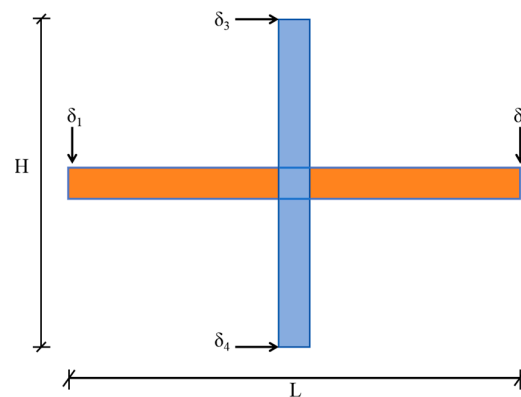

Figure 18. The schematic diagram of the relationship between the layer shear force and the interlayer displacement angle of the joint specimen.
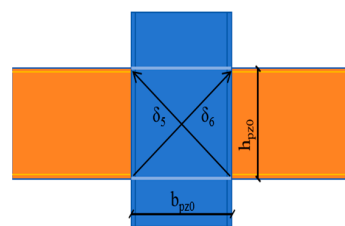

Figure 19. Schematic diagram of panel zone shear ratio.

As shown in Figure 21a–c, the hysteresis curves of the specimens B345-T16-BFW-1 and B345-T16-BFW-2 are relatively full, display no obvious pinch shrinkage phenomenon, and they exhibit a better energy dissipation capability. The hysteresis curve of specimen B345-T16 displays the phenomenon of pinch shrinkage, and the energy consumption is relatively lower than the flange of the weakened steel beam specimen, and the three specimens have different degrees of decline in the story drift ratio of 4%, which is due to the flexure of the beam flange at the beam-end shrinkage region and the bulging in the web plate, which leads to a more significant reduction in the load carrying capacity. As shown in Figure 21d,e, the hysteresis curves of the steel beam open circular web hole-type joint and the open honeycomb hole-type joint display the phenomenon of pinch shrinkage. The joint's energy dissipation is poor, and it reaches the ultimate load when the ratio of the story drift ratio reaches 3%, the subsequent out-of-plane

deformation of the web in the open hole area is obvious, and a plastic hinge occurs in the area of the beam-end open holes, which leads to a significant decrease in the carrying capacity, and the joint's load carrying capacity decreases to the ratio of the story drift ratio, reaching 5%, which leads to a significant decrease in the joint's load carrying capacity. When the load carrying capacity is 70.2% of the ultimate load, this indicates that the joint has been damaged.
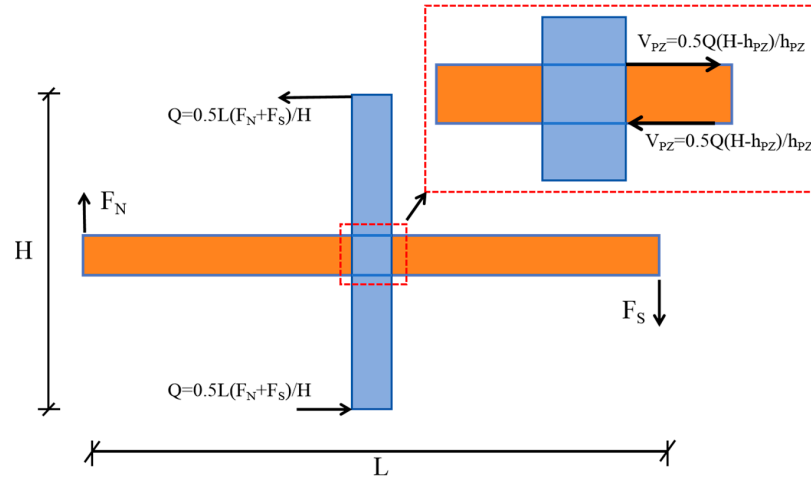

Figure 20. The schematic diagram of the force on the joint specimen of FEM model.
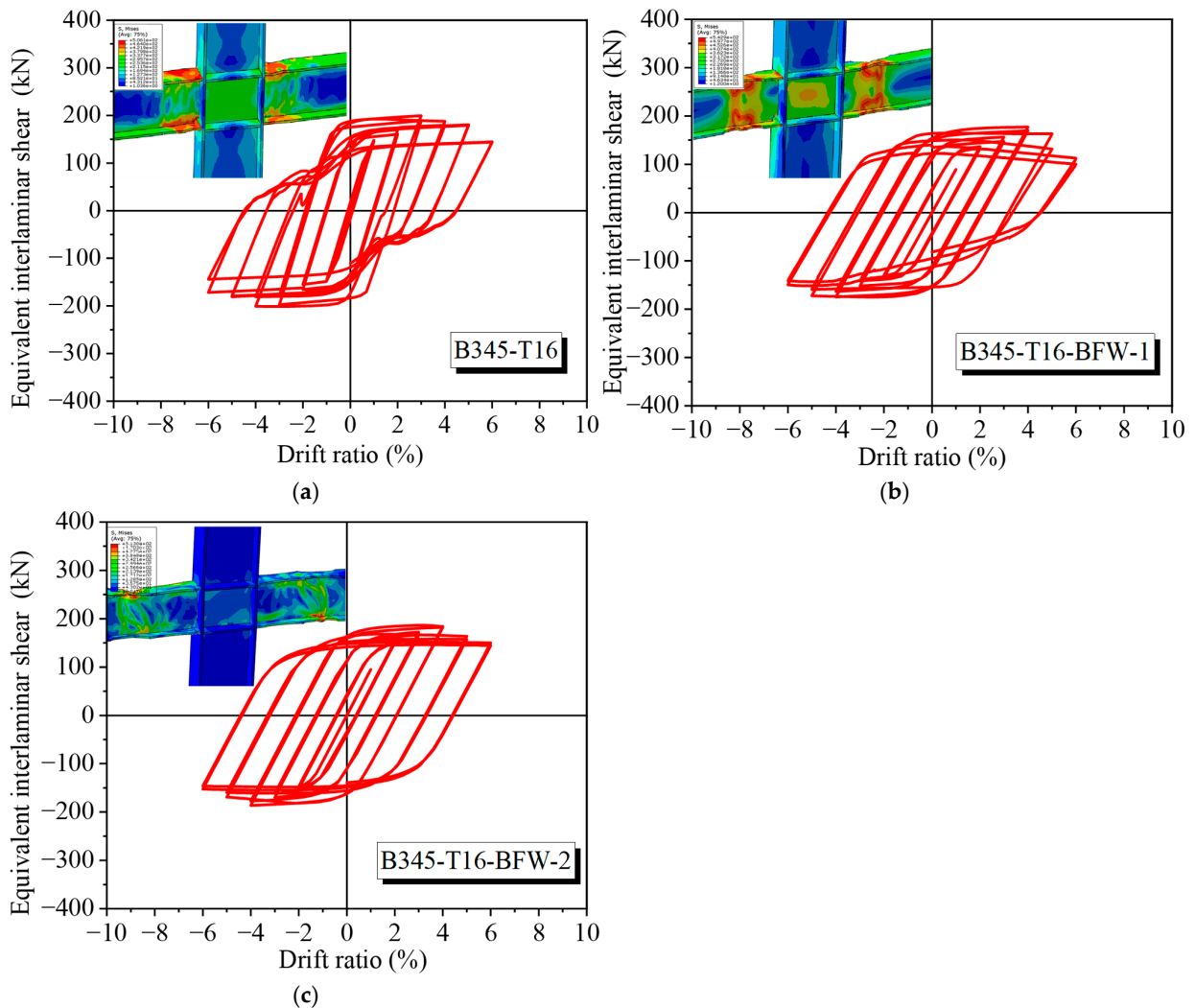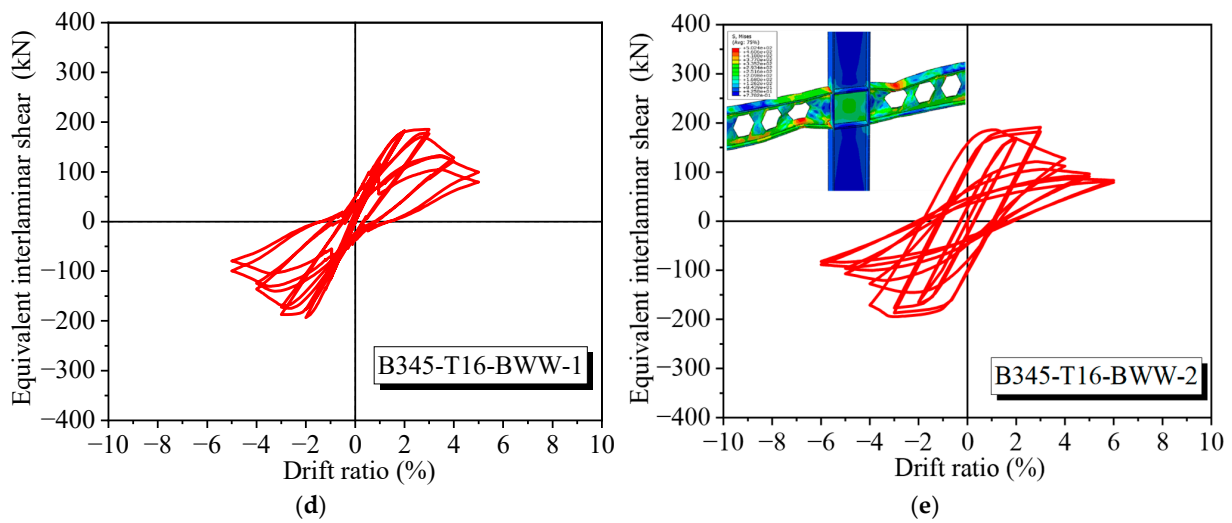

Figure 21. *Cont.*

(d)

(e)

Figure 21. Equivalent inter-story shear load–drift ratio curve of joint specimen: (**a**) B345-T16; (**b**) B345-T16-BFW-1; (**c**) B345-T16-BFW-2; (**d**) B345-T16-BWW-1; (**e**) B345-T16-BWW-2.

3.3.3. The Moment–Shear Ratio Curves of Joint in Panel Zone

Through the force on the specimens as shown in Figure 22, based on the beam-end load FN and FS, as well as the equilibrium relationship in the figure, one can calculate the equivalent bending moment sustained by the panel zones $M_{PZ} = V_{PZ}h_{PZ}$, and combined with the shear ratio of the panel zone calculated from Equation (5), the bending moment–shear ratio of the panel zone (M_{PZ}-θ_{PZ}) curves for each group of joint can be obtained, and are shown in Figure 22.

It can be clearly observed from Figure 22, in specimen B345-T16 in the loading process, the deformation and energy dissipation provided by the panel zone is much larger than for the other four specimens; the maximum shear ratio can reach 0.38, while for the edge weakening of specimens B345-T16-BWW-1 and B345-T16-BWW-2, the panel zone maximum shear ratio is only 0.18 and 0.16, and for the open web hole-type specimen B345-T16-BFW-1, this is only 0.008.
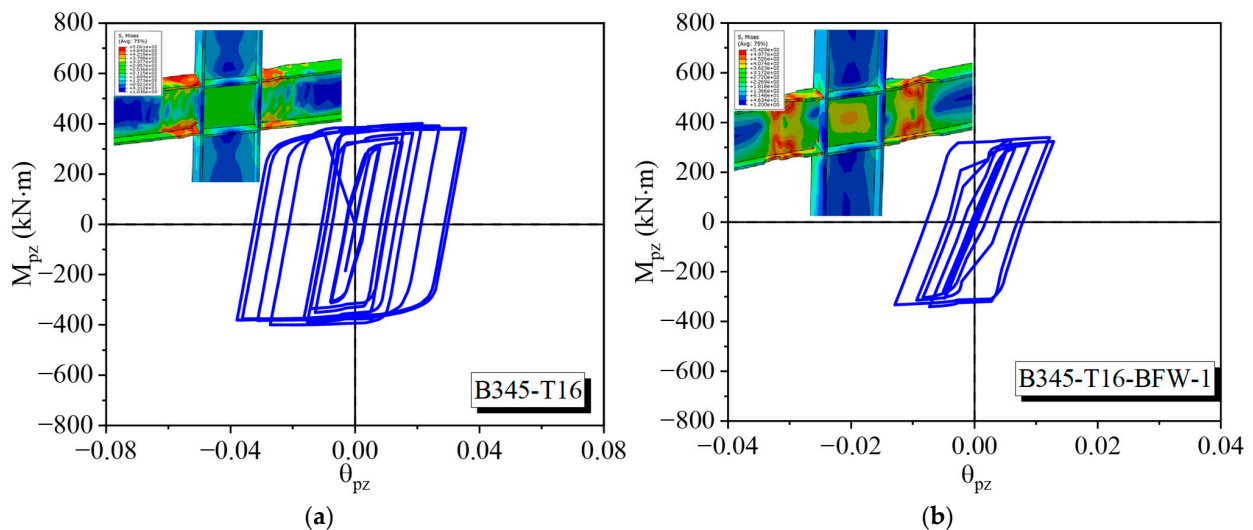

(a)

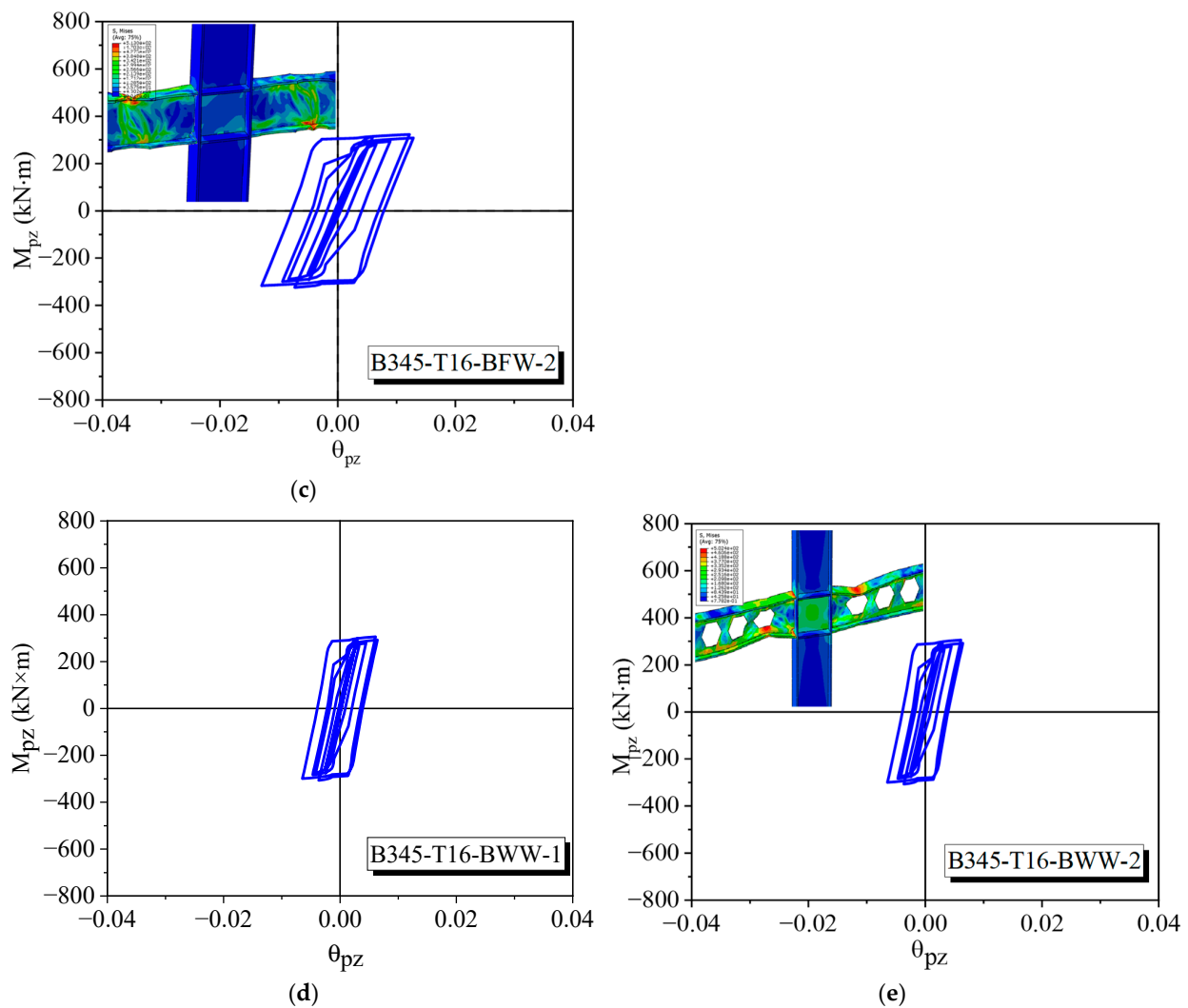**(b)**

Figure 22. *Cont.*

Figure 22. Moment–shear ratio curves for joint specimens in panel zone: (**a**) B345-T16; (**b**) B345-T16-BFW-1; (**c**) B345-T16-BFW-2; (**d**) B345-T16-BWW-1; (**e**) B345-T16-BWW-2.

The results show that the beam end of the steel beam weakened flange and weakened web opening-type specimens bear the majority of the deformation and energy dissipation of the whole joint, while the panel zone participation in the energy dissipation of the web opening-type specimens T14-BWW-1 and T14-BWW-2 accounts for a much smaller percentage; the web deformation of the steel beam is too large during the loading process, serious buckling occurs, the joint bearing capacity decreases dramatically, and the deformation produced by the steel beam takes up all of the deformation and energy dissipation of the joint, and also the energy dissipation of the panel zone is much worse.

3.3.4. Stress Transfer and Distribution Law of Steel Beam Flange

Cells with distances of 5 mm, 75 mm, 215 mm, 335 mm, 495 mm, 635 mm, 685 mm, and 735 mm are taken along the length of the steel beams to output the Mises stresses in the elastic and plastic, as well as destructive, phases of the above-mentioned cells, which are shown in Figure 23.
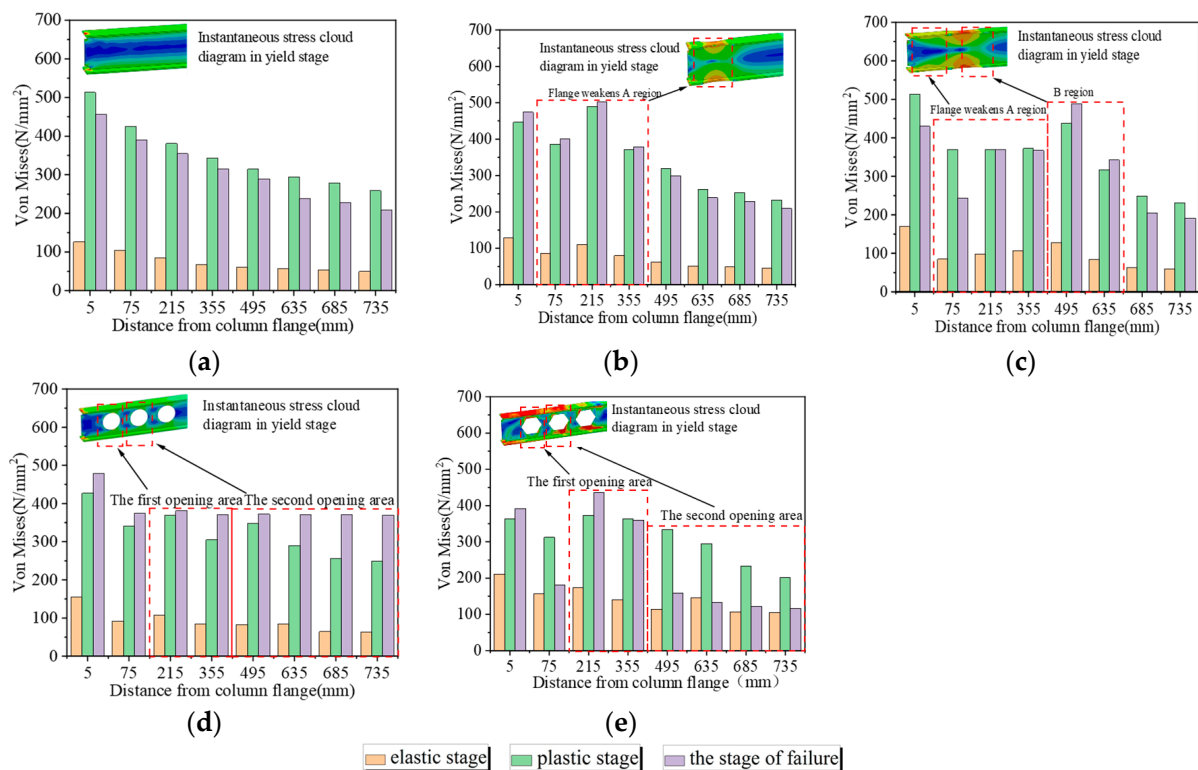
Figure 23. Steel beam flange stress distribution: (**a**) B345-T16; (**b**) B345-T16-BFW-1; (**c**) B345-T16-BFW-2; (**d**) B345-T16-BWW-1; (**e**) B345-T16-BWW-2.

For example, in Figure 23a–c, the stress diagrams of three joints, B345-T16, B345-T16-BFW-1, and B345-T16-BFW-2, it can be clearly seen that the girder unit closing to the flange of the column exhibits higher stress. Only for the RBS joint with a weakened flange in region I, is the output stress of the beam unit 215 mm away from the column flange during loading higher than the surrounding stress value, and smaller than the unit stress at the butt location of the flange both in the beam and column. The DRBS joint in the weakened flange region II clearly displays the stress concentration phenomenon, the region I beam flange reduction c1 value is smaller than that of the region II flange reduction c2 value, and the 215 unit stress is greater than 75 units in the unweakened region, but due to the increased degree of weakening in region II, the stress here is greater than in the former region, with the greater the distance from the column flange, the lower the unweakened beam cross-section stress gradually becomes. The beam web opening type-BWW-1 and -BWW-2 joints provide the highest unit stress in the area of the column and beam flange buttresses, and with the increase in the distance, the stress decreases; in the flange portion of the region of the first openings from the beam end, there is a concentration of stress, and the stress value is greater than the stress value at the flange near it.

3.3.5. Distribution Law of Equal Stress of Panel Zone

As depicted in Figure 24, DE and BC, which are two stress paths, are taken in the nodal region to investigate the stress development and distribution patterns of the panel zone. In this section, a comparative analysis is carried out for the equivalent stress development of the unit on stress path 1. Figure 25 shows the stress development trend at point A in the center of the B345-T14 panel area.
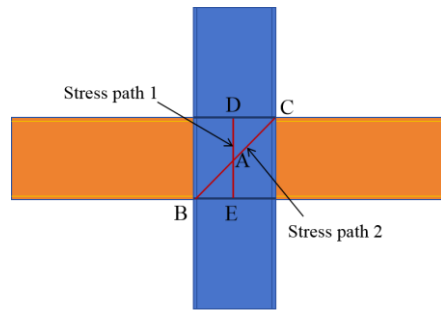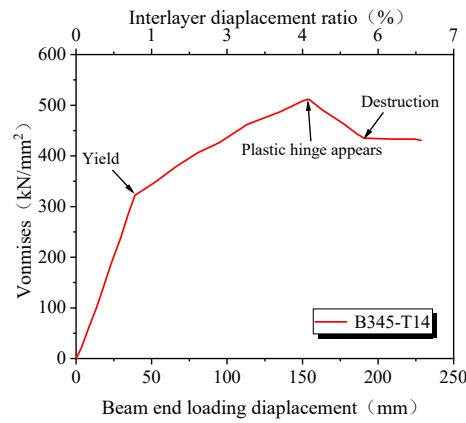
Figure 24. Unit stress extraction path.

Figure 25. Mises stress at point A in the center of the B345-T14 panel zone.

As shown in Figure 26, the unit equivalent stresses along stress path 1 for five sets of specimens, B345-T16, B345-T16-BFW-1, B345-T16-BFW-2, B345-T16-BWW-1, and B345-T16-BWW-2, are shown.
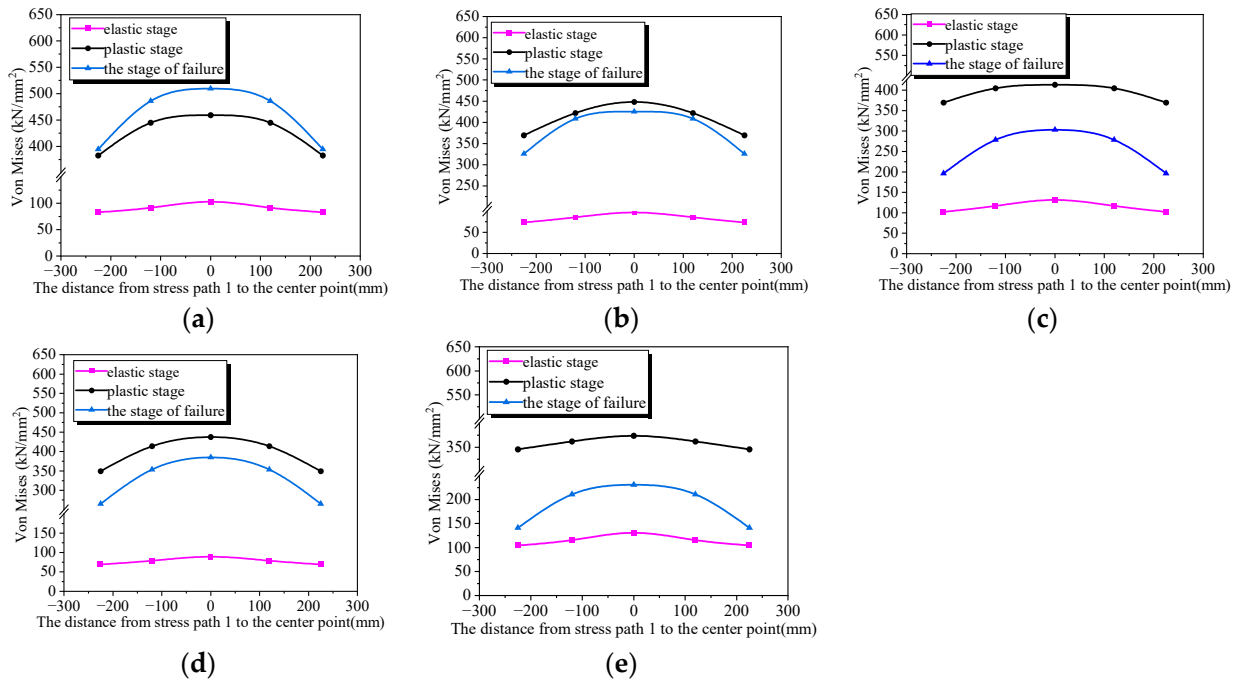

Figure 26. Equal force of joint in path 1: (**a**) B345-T16; (**b**) B345-T16-BFW-1; (**c**) B345-T16-BFW-2; (**d**) B345-T16-BWW-1; (**e**) B345-T16-BWW-2.

As shown in Figure 26, the equivalent stress values of the five groups of joints in the elastic, yield, and damage stages along stress path 1 of the panel zone are shown, and the horizontal coordinates in the figure are the relative distances between each cell selected on path 1 and the panel zone center, point A.

During the elastic stage, the distribution of stress between the five specimens is relatively analogous, and the stress in the center panel zone of specimens B345-T16, B345-T16-BFW-1, and B345-T16-BFW-2 is the largest; the stress values at the two sides are smaller, with maximum stresses of 103.01 MPa, 76.78 MPa, and 154.05 MPa, respectively; and specimens B345-T16-BWW-1 and B345-T16-BWW-2 show maximum stress values of 131.61 MPa and 130.75 MPa in the panel zone during the elastic phase.

When in the yielding stage, the maximum stress at the center point A of specimens B345-T16, B345-T16-BFW-1, and B345-T16-BFW-2 are all more than 500 MPa, with the stress at the center point of the panel zone in specimen B345-T16 being greater than that in the other two specimens. The maximum Mises equivalent stresses reached at the center point of the panel zone of specimens B345-T16-BFW-1 and B345-T16-BFW-2 in the yield stage were 413.34 MPa and 373.83 MPa.

After the damage stage, due to the rapid expansion of the steel beam deformation of the specimen with the beam-end displacement increasing, the stiffness of the steel beam decreases continuously and generates stress redistribution, resulting in a decrease in the effective stress at the center of the panel zone; the stress at the pivot point of specimens B345-T16-BFW-2 and B345-T16-BFW-3 decreases by 94.91% and 87.95%, respectively. The center point stresses of specimens BWW-1 and BWW-2 decreased by 73.28% and 61.73%, but the center point stresses of the panel zone of specimen BFW-2 increased by 110.95% compared to the yield stage.

From the comparison of the three stages of elasticity, yielding, and damage of the five groups of specimens, it can be clearly seen that the overall effective stresses in the panel zone of the BWW-type and BFW-type joint specimens are at a lower level, which indicates that the RBS joints, DRBS joints, and the open hole-type joints of the beam webs form plastic hinges with the end of the beams, which can effectively reduce the stresses in the panel zone to prevent the emergence of plastic hinges in the panel zone, in order to achieve the goal of weak beams and strong columns and strong joints and weak components.

3.3.6. Distribution Law of Shear Stress in Panel Zone

In the loading process, the panel zone mainly bears the shear force; this section is selected as the unit shear stress in path 2. The five groups of specimens in each displacement loading stage of the shear stress are compared, and in the figure, the vertical coordinate is used to select the joints from the center of the relative height of point A, and the horizontal coordinate represents the finite element model's results of the unit shear stress and the panel zone shear yield strength, where the shear yield strength of the panel zone is calculated according to the following equation:

$$\tau = \frac{f_y}{\sqrt{3}} \tag{6}$$

Note: τ is the yield shear strength for steel; f_y is yield strength for steel.

As shown in Figure 26, the shear stress ratio in stress path 2, the vertical direction of the panel zone, and the shear yield strength of the panel zone obtained according to Equation (6) are shown for the five sets of specimens: B345-T16; B345-T16-BFW-1; B345-T16-BFW-2; B345-T16-BWW-1 and B345-T16-BWW-2.

As shown in Figure 27a–e, for the five groups of specimens in stress path 2, the panel zone vertical direction shear stress distribution is more uniform.
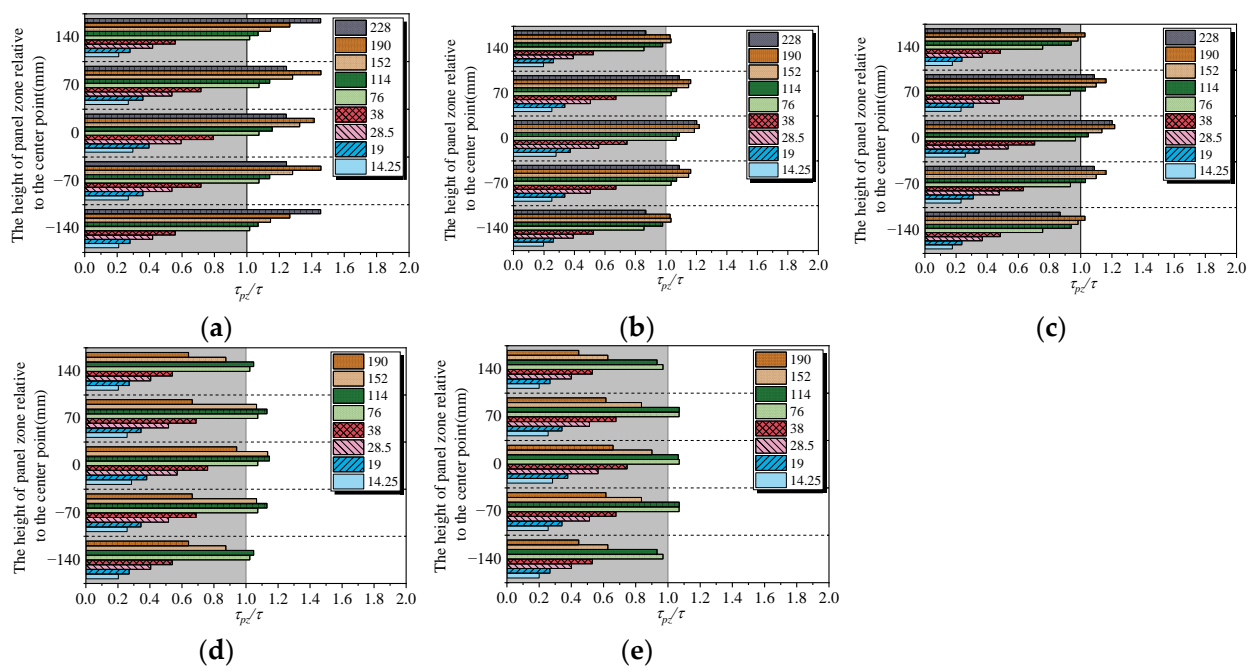
Figure 27. Shear stress of joint in path 2: (**a**) B345-T16; (**b**) B345-T16-BFW-1; (**c**) B345-T16-BFW-2; (**d**) B345-T16-BWW-1; (**e**) B345-T16-BWW-2.

When the displacement amplitude is at 14.25–38 mm, specimen B345-T16's panel zone region did not reach the yield strength; the maximum shear stress at the center point is 0.79 times the steel shear yield strength, and when the displacement reaches 76 mm, the panel zone of the overall region is in the yield stage, indicating that the panel zone has yielded. With the displacement increasing, the panel zone shear stress continues to increase, and the story displacement reaches 228 mm. With the displacement increasing, the shear stress in the panel zone continues to increase, and when it reaches 228 mm and the ratio of story displacement reaches 6%, the panel zone center as well as a small range of shear stress in the vicinity appears to fall.

When the displacement amplitude is 14.25–38 mm, the maximum shear stress of the panel zone of joint B345-T16-BFW-1 also does not reach the shear yield strength, but when the slip of the beam reaches 76 mm, the specimen B345-T16-BFW-1 reaches the shear yield strength only at the center point and the nearby area, and the whole area of the panel zone reaches the yield strength when the displacement continues to increase up to 152 mm, and the ratio of the story drift ratio reaches 4%. When the displacement continues to increase to 152 mm, and at a story drift ratio of 4%, the whole region of the panel zone reaches the shear yield strength, and then the shear stress continues to rise with the increase in displacement, and the plastic hinge deformation of the beam end increases and the shear stress of the panel zone appears to fall after the ratio of the story drift ratio reaches 6%.

When the displacement amplitude is 14.25–76 mm, the panel zone of specimen B345-T16-BFW-2 does not yield, as depicted in Figure 27c, and the maximum shear stress at the center point is 0.97 times the shear yield strength. The panel zone reaches the shear yield strength at the center point when the displacement amplitude is 114–152 mm, and continues to be loaded to 190 mm, i.e., the shear yield strength is reached across the panel zone at a story drift ratio of 5%, which indicates that the panel zone as a whole enters the yielding stage, and the shear stresses start to fall after the displacement of the beam end reaches 228 mm.

Comparing the distributions of the shear stress in specimens B345-T16-BWW-1 and B345-T16-BWW-2 under each loading level, it can be seen from Figure 27d,e that both specimens remain in the elastic stage as the slip amplitude enters the range of 14.25–38 mm, and the maximum shear stresses at the center point are 0.76 and 0.74 times the shear yield

strength. At a displacement amplitude in the range of 76–114 mm, specimen B345-T16-BWW-1 reaches the shear yield strength across the entire the panel zone, while specimen B345-T16-BWW-2 reaches the shear yield strength only in the center point and within this vicinity. As the displacement continues to load, due to the expansion of the web surface deformation at the beam end, the panel zone shear stress begins to decline, in which specimen B345-T16-BWW-2's shear stress decline is greater than that of the other specimens.

From the distribution of the panel zone shear stresses of the above five groups of specimens at each loading level, it can be seen that the DRBS joints can effectively reduce the panel zone shear stresses and delay the panel zones from entering the yielding stage. Also, the DRBS joints are more effective than the other ones, and the BWW type also has an effect on the distribution law of the panel zones, and the panel zones shear stresses of T16-BWW-1 are lower than those of T16-BWW-2 in general.

3.3.7. Ultimate Load and Ductility Coefficient

Ductility effectively reflects the structural deformation ability, which is an important index for evaluating the seismic performance of building structures. In this paper, the ductility of H-type beam–column joints is evaluated by calculating the displacement ductility coefficient. The yield, ultimate load, and ductility coefficient of the specimens are given in Table 6.

Table 6. Limit load and displacement ductility factors.

Serial Number	Yield Displacement Δ (mm)	Yield Load P_y/kN	Limit Displacement Δ_y (mm)	Ultimate Load P_y (kN)	Ductility Factor μ
B345-T16	90.06	176.29	211.66	204.73	2.35
B345-T16-BFW-1	80.56	155.49	201.02	157.33	2.49
B345-T16-BFW-2	83.60	178.27	222.68	106.25	2.66
B345-T16-BWW-1	74.86	167.80	164.92	109.93	2.21
B345-T16-BWW-2	71.44	125.92	175.56	94.65	2.46

The displacement ductility coefficient μ of the joint is the ratio of the beam-end displacement δ_u when the joint is destroyed to the beam-end displacement δ_y when the joint is yielded, which can be calculated according to the following formula:

$$\mu = \frac{\delta_u}{\delta_y} \tag{7}$$

From Table 6, it can be seen that beam-end flange weakening and web opening have a considerable impact on the ductility of the joint. The ductility coefficient of specimen B345-T16 is 2.35, and for the RBS joint specimen B345-T16-BFW-1, which has only one region of beam flange weakening, the ductility coefficient is increased by 1.06 times, while specimen B345-T16-BFW-2 is a DRBS joint, and the beam flange weakening of the double region involved in the deformation improves the joint's ductility, where the ductility coefficients are increased by 1.13 and 1.07 times compared to the first two specimens. The ductility coefficients of specimens B345-T16-BWW-1 and B345-T16-BWW-2 with beam web openings of circular holes and honeycomb holes are 2.21 and 2.46, which is due to the fact that the concentration of stress at the corner of the honeycomb holes in the web occurs more easily than that of the circular holes, which further causes the flexural deformation of the beam web and the generation of plastic hinges at the end of the beams, and the deformation of the steel beams occupies almost all of the deformation of the joint.

3.3.8. Degradation of Stiffness

The stiffness degradation coefficient is the absolute ratio of the degraded stiffness under each displacement loading to the illustrated stiffness in the initial elastic loading stage. The corresponding tangent stiffness of the specimen under each level of displacement

loading is calculated, as shown in Table 7, and the resulting diagram of the stiffness degradation coefficient is shown in Figure 28.

Table 7. The tangent stiffness values under each level of displacement loading.

| Displacement Amplitude/mm	−14.25	−19	−28.5	−38	−76	−114	−152	−190	−228
T16-BFW-1	2.67	2.67	2.67	2.67	2.24	1.57	1.31	1.23	0.91
T16-BFW-2	2.50	2.50	2.50	2.50	1.99	1.42	1.17	0.84	0.64
T16-BWW-1	2.56	2.56	2.56	2.56	2.21	1.55	1.12	0.51	—
T16-BWW-2	2.54	2.54	2.54	2.54	1.94	1.37	0.75	0.44	—
Displacement Amplitude/mm	14.25	19	28.5	38	76	114	152	190	228
T16-BFW-1	2.67	2.67	2.67	2.67	2.26	1.61	1.41	1.10	0.90
T16-BFW-2	2.50	2.50	2.50	2.50	2.02	1.46	1.21	0.83	0.63
T16-BWW-1	2.56	2.56	2.56	2.56	2.23	1.60	0.74	0.48	—
T16-BWW-2	2.54	2.54	2.54	2.54	2.00	1.35	0.67	0.42	—
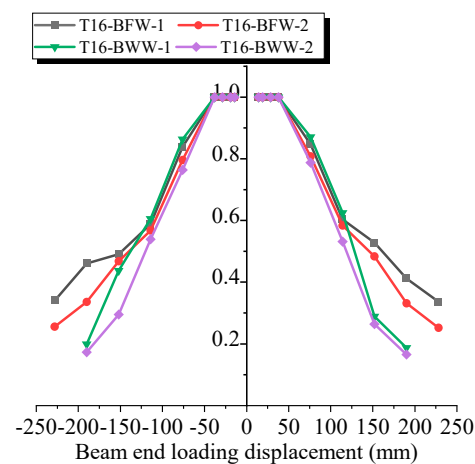
Figure 28. Stiffness degradation coefficient curve.

The joint stiffness degradation mainly goes through two stages: the first stage is a short flat section, in which all joints are in the elastic deformation stage, and no stiffness degradation phenomenon occurs; the second stage is a decreasing curve section, in which the deformed joint stiffness starts to decrease after the yielding of the member.

From the combination of Table 6 and Figure 28, the stiffness degradation coefficient curve can be seen.

When the displacement of the beam end is 14.25 to 38 mm, the stiffness degradation coefficient of the specimens B345-T16, B345-T16-BFW-1, B345-T16-BFW-2, B345-T16-BWW-1, and B345-T16-BWW-2 is basically unchanged. After reaching 76 mm, the stiffness degradation coefficient begins to decrease, and the slope of the curve gradually decreases with the increase in displacement. The magnitude of the stiffness degradation coefficient of specimens B345-T16, B345-T16-BFW-1, and B345-T16-BFW-2 decreases with displacement reaching 114 mm, and for specimens B345-T16-BWW-1 and B345-T16-BWW-2, the slope of the stiffness degradation coefficient curve decreases when the beam-end displacement reaches 152 mm, and the inter-story displacement angle ratio is 4%. The slope of the curve increases with the increase in displacement. After that, the slope of the stiffness degradation factor curve begins to decrease.

According to the overall stiffness of the joint sorted as T16 > BFW-1 > BFW-2, in the process of beam-end displacement loading, the weakened area of the steel beam of specimen B345-T16-BFW-1 displays stress concentration and buckling deformation, because the stiffness of the RBS joint depends on the stiffness of the beam and the weakening of

the flange reduces the initial stiffness of the steel beam; since the stiffness of the RBS joint depends on the stiffness of the beam, the weakening of the flange reduces the initial stiffness of the beam. The faster the stiffness degradation of the joint, the faster the stiffness degradation coefficient decreases.

The stiffness degradation rate of specimens B345-T16-BWW-1 and B345-T16-BWW-2 is faster, and the overall stiffness coefficient of the joint is smaller than that of the beam-end flange weakening specimen. Since the honeycomb-type opening of its steel beam web opening rate is slightly larger than the former, the overall stiffness degradation coefficient of joint B345-T16-BWW-2 is larger than that of joint B345-T16-BWW-1 in the decreasing section of the stiffness degradation coefficient curve.

3.3.9. Equivalent Viscous Damping Coefficient

The energy dissipation capacity of the joint can be expressed by the equivalent viscous damping coefficient. The equivalent viscous damping coefficient is calculated according to the principle of the equivalent damping force. The damping ratio of the whole specimen under a certain displacement state in the whole loading system can represent the energy dissipation capacity of the specimen. It could be calculated according to the ratio of the area S_1 surrounded by the largest hysteresis loop semicircle ABC and the abscissa to the area S_2 of the triangular OBD in the hysteresis curve in Figure 29. The equivalent viscous damping coefficient is calculated as follows:

$$\xi_e = \frac{1}{2\pi} \times \frac{S_1}{S_2} = \frac{1}{2\pi} \times \frac{S_{curveOABCO}}{S_{\triangle OBD}} \tag{8}$$
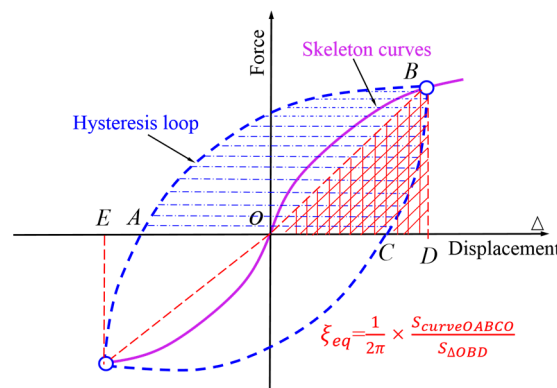

Figure 29. Calculation of equivalent viscous damping coefficient.

As shown in Figure 30, the steel beam flange weakening and web opening have an important impact on the joint energy dissipation. The following conclusions can be obtained from the figure:
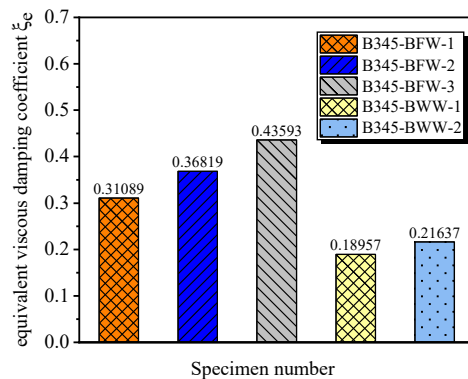

Figure 30. Equivalent viscous damping coefficient of the specimen.

(1) The equivalent viscous damping coefficients of specimens B345-T16, B345-T16-BFW-1, and B345-T16-BFW-2 are more than 0.3, which indicates that the steel beam flange weakening could highly improve the energy dissipation of the specimen. As the degree of beam flange weakening increases, the energy dissipation capacity increases significantly, and the energy dissipation of the beam flange-type joint with DRBS is the best, and its equivalent viscous damping coefficient is 1.39 and 1.16 times that of specimens B345-T16 and B345-T16-BFW-1.

(2) The equivalent viscous damping coefficients of specimens B345-T16-BWW-1 and B345-T16-BWW-2 are 0.19 and 0.22, and the web honeycomb hole-type joint exhibits better energy dissipation compared to the open circular web hole-type joint.

4. Conclusions

In this work, five sets of specimens, B345-T16, B345-T16-BFW-1, B345-T16-BFW-2, B345-T16-BWW-1, and B345-T16-BWW-2, were numerically simulated, and the impact of the weakening of the panel zone in terms of the seismic behavior of the joints was studied through analyses of the stress cloud, the distribution of the Mises equivalent stresses and shear stresses in the panel zone, the distribution of the steel beam flange stresses, the equivalent shear force–drift ratio curves, skeletal curves, moment–shear ratio curves of the panel zone, and the coefficients of ductility, and the following conclusions could be obtained as follows:

(1) For joint B345-T16-BFW-1, the plastic hinge was generated in the first reduction area of the beam flange, 215 mm from the column's end. For joint B345-T16-BFW-2, the plastic hinge was generated in the second reduction area of the beam flange, 495 mm from the column's end. Compared with the RBS joint, the plastic hinge of the DRBS joint was shifted further outward. This prevented the butt joint of the beam–column flange from cracking and causing premature damage. Both joints achieved the purpose of plastic hinge outward movement.

(2) The DRBS joint exhibited more complete hysteresis curves and a higher load bearing capacity than the RBS joint. In particular, the ultimate load bearing capacity, ductility, and equivalent viscous damping coefficient of the DRBS joint were increased by 10.78%, 6%, and 6%, respectively, compared to the RBS joint. Additionally, the load bearing capacity of the DRBS joint decreased slower and the joint stiffness degraded slower. The finite element simulation verified that the DRBS joint exhibited superior plastic hinge outward movement characteristics, avoiding the brittle damage of the beam–column joint welds and exhibiting good seismic performance.

(3) Compared with the web opening-type joints, the honeycomb opening-type joints exhibited an increase in ductility and the equivalent viscous damping coefficient of 11.31% and 15.79%, respectively, but a decrease in the ultimate load carrying capacity of 17.83%.

(4) The weakened DRBS flange joint and steel beam honeycomb hole-type joint mainly rely on the beam to bear deformation and dissipate energy. During the entire loading process of the joint specimen, the stress of the joint domain remains at a low level, and the joint domain dissipates energy at a small proportion, which means it fails to take advantage of the energy dissipation from the panel zone after entering the yield stage.

Data Availability Statement: The original contributions presented in the study are included in the article.

References

1. Cao, J.H.; Hao, J.P.; Xue, Q.; Fan, C.L.; Sun, X.L. Seismic behavior of wall-type spiral stirrups-confined RC column to steel beam joint. *J. Constr. Steel Res.* **2023**, *210*, 108051. [CrossRef]
2. Simões, D.S.L.; Hélder, C.; Jorge, C.; Rui, S.; Catinaccio, A.; Dimitar, M.; Batista, L.J.; Alvarez, F.D.; Christophe, B. Experimental behaviour of large-size beam-to-column steel joints for the DUNE Neutrino Experiment. *Thin-Walled Struct.* **2023**, *19*, 110996. [CrossRef]
3. Li, Y.Q.; Huang, B.H. Research on load-bearing performance of new fabricated steel structure beam-column joints with energy dissipating elements. *Structures* **2022**, *38*, 492–501. [CrossRef]
4. Liu, R.Y.; Wang, H.; Yan, G.Y.; Wu, J.; Lai, Q.L. Numerical study on the seismic performance of the damage-control beam-to-column joint with artificial steel hinge. *J. Constr. Steel Res.* **2024**, *212*, 108313. [CrossRef]
5. Nie, S.D.; Li, J.Y.; Wang, H.; Deng, Y.Z.; Chen, Z.Y.; Elchalakani, M.; Liu, M. Seismic behavior of welded high-performance steel beam-to-column joints with different reinforced configurations. *J. Constr. Steel Res.* **2023**, *210*, 108113. [CrossRef]
6. Tong, L.W.; Zheng, J.M.; Wu, H.L.; Wang, K.Y.; Dong, B.P.; Liu, B. Parametric study of steel-beam to flat-rectangular CFST column connections with small-size diaphragms. *J. Constr. Steel Res.* **2023**, *211*, 108156. [CrossRef]
7. Wang, H.; Hao, J.; Xue, Q.; Sun, X. Seismic behaviour of a wall-type concrete-filled steel tubular column with an end plate steel beam reinforced joint. *Soil Dyn. Earthq. Eng.* **2023**, *173*, 108142. [CrossRef]
8. Zhong, Y.L.; Li, G.Q.; Xiang, Y.; Wang, Y.B. Seismic behavior of steel beam-column connection with assembled steel rod energy dissipaters. *J. Build. Eng.* **2023**, *76*, 107037. [CrossRef]
9. Tsai, K.C.; Wu, S.; Popov, E.P. Experimental performance of seismic steel beam-column moment joints. *J. Struct. Eng.* **1995**, *121*, 925–931. [CrossRef]
10. Zhou, W.; Li, B.S.; Zhao, G.T.; Gao, C. Experimental study of seismic performance of PEC column-steel beam 3D frame with endplate connection. *J. Constr. Steel Res.* **2023**, *202*, 107765. [CrossRef]
11. Pan, L.L.; Chen, Y.Y.; Jiao, W.F.; Chuan, G. Experimental study on panel zone in spatial H-shaped beam-column connections under cyclic loading. *J. Build. Struct.* **2015**, *36*, 11–19.
12. Pan, L.L.; Chen, Y.Y. Modified formula for calculating elastic stiffness of panel zone in H-Shaped Beam-Column Connections. *Eng. Mech.* **2016**, *33*, 68–74+94.
13. Brandonisio, G.; De Luca, A.; Mele, E. Shear strength of panel zone in beam-to-column connections. *J. Constr. Steel Res.* **2012**, *71*, 129–142. [CrossRef]
14. Amani, R.; Saffari, H.; Fakhraddini, A. Local Flange Bending and Continuity Plate Requirements in Double-Web H-Shaped Columns. *Int. J. Steel Struct.* **2018**, *18*, 199–209. [CrossRef]
15. Wang, H. Study on the Effect of the Deformation of Panel Zones on the Steel Rigid Frames Response. Master's Thesis, Xi'an University of Architecture and Technology, Xi'an, China, 2004.
16. Ren, Y.R. Research on Flange Reinforced Plane Zone at Beam-End. Master's Thesis, Qingdao University of Technology, Qingdao, China, 2010.
17. El-Tawil, S.; Vidarsson, E.; Mikesell, T.; Kunnath, S.K. Inelastic Behavior and Design of Steel Panel Zones. *J. Struct. Eng.* **1999**, *126*, 183–193. [CrossRef]
18. Yang, T. Research on Mechanical Properties at Panel Zone of Steel Frame Reinforced Conncetion. Master's Thesis, Qingdao University of Technology, Qingdao, China, 2014.
19. Chen, F. Research on How the Thickness of Joint Zone Affects the Mechanical Performance of Steel Joint. Master's Thesis, Liaoning University of Technology, Jinzhou, China, 2014.
20. Deylami, A.; Moslehi, T.A. Effect of column panel zone characteristics on instability of beams with RBS moment resisting connections. In Proceedings of the 13th World Conference on Earthquake Engineering, Vancouver, BC, Canada, 1–6 August 2004.
21. Chen, Y.A. Research on Seismic Damage Control of Welded High Strength Steel Beam-Column Joints. Master's Thesis, Institute of Engineering Mechanics, China Earthquake Administration, Beijing, China, 2019. (In Chinese).
22. Wang, L.Y. Study on Seismic Behavior of Steel Frame Beam-Column Modified Rigid Joints. Master's Thesis, Beijing Institute of Building Engineering, Beijing, China, 2011. (In Chinese)
23. *ANSI/AISC 361-10*; Specification for Structural Steel Buildings. American Institute of Steel Construction: Chicago, IL, USA, 2010.